

Aligned cellulose nanocrystals thin films

by Levente Csóka

Dissertation submitted to the Hungarian Academy
of Sciences, in partial fulfillment of the requirements
for the degree of Doctor of the Hungarian Academy
of Sciences

April 2016

Sopron, Hungary

To K.

Preface

Cellulose nanocrystals (CNCs) owes much of its versatility to its surface characteristics and molecular structure, as these can be tailored to a variety of applications. Characterizing and controlling these properties with sophisticated tools is central to thin-film formation and piezoelectric product development. Our intent in compiling this work is to provide the collective experience of cellulose nanocrystal manipulation at nano scale level and film formation for new product development. We hope that the book will allow the reader to quickly understand the used theory in a given problem. Results and the advanced models described may be applied to understand and control the alignment of CNCs during film formation and piezoelectric, static energy harvesting applications. Furthermore, the scientific background of calculated polarizability of prolate objects in aqueous solution was used to describe electrophoretic phenomena of CNCs subjected to electric fields are also discussed. Moreover quantum-mechanical calculation is performed on basic crystal structure of cellulose for polarization calculation as well. The body of this work is organized into five numbered chapters based on our recently published, but significantly supplemented articles. Chapter I, the General Introduction provides limited information to readers who are less familiar with the unique characteristics of cellulose and cellulose nanocrystals. Chapters II-IV are stand-alone documents with the supplemented works, containing all the necessary sections including references. Chapter V contains an overall summary and the conclusions in the form of theses. There are few individuals who contributed to these works. They are mentioned by name in the Acknowledgements section. Nonetheless, to salute those who provided scientific and physical help, encouragement, friendship and love during the course of this undertaking, the plural version “we” is practiced in this write-up.

Levente Csóka

Acknowledgement

Special recognition for Dr. Ilona Peszlen, Dr. Perry Peralta and Dr. Orlando Rojas at Institute of Forest biomaterials at North Carolina State University, Raleigh, NC and Dr. George Grozdits at Louisiana Tech University should receive for their valuable contributions to my postdoctoral research, resulting in a number of great publications. They provided the opportunity to compliment my postdoctoral education in a research oriented, challenging environment.

I would like to express my deepest gratitude to Dr. Vladimir Djokovic, who supervised my scientific work from Vinca Institute of Nuclear Sciences, deserves tremendous credit for his gifted, scientific mind and for his friendship towards me. He was always tireless for providing guidance in the “jungle” of technical writing in English.

I am indebted to Prof. Josef Makovitzky at Institute of Anatomy II, Jena, who introduced me the human amyloid structure giving an opportunity to working with him on Alzheimer disease observation with carbohydrate fibril's histochemistry studies.

Partners and colleagues at the University of West Hungary, Sopron included: Drs. Ferenc Divós, László Elek, András Winkler, Róbert Németh, Péter Takáts and Tibor Alpár, Gábor Dóka at Aqua-Filt Ltd and Ottó Kolonics at celltech-paper Ltd. Without their significant contributions, many of our Institutional projects would not have been possible.

Dr. Katalin Halász, Dr. Veronika Nagy and Dr. Dimitrios Tsalagkas former graduate students - should receive enormous appreciation for their exceptional research work during the course of their studies. Their attitude made my life as a faculty member more bearable.

Table of content

Chapter 1 – General introduction	5
1.1. References	14
Chapter 2 – Dielectrophoresis of cellulose nanocrystals	16
2.1. Introduction	16
2.2. Materials and methods	17
2.2.1 Materials	17
2.2.2 Preparation of CNC films.....	18
2.3. Theoretical consideration	20
2.4. Results and discussion.....	28
2.5. CNC polarization using quantum-mechanical approach	40
2.6. Conclusion	44
2.7. References	45
Chapter 3 – Ultrathin piezoelectric films of cellulose nanocrystals.....	48
3.1. Introduction	48
3.2. Materials and methods	51
3.2.1. Cellulose Nanocrystals.....	51
3.2.2. Manufacture of CNC films.....	51
3.3. Piezoelectric measurement	53
3.4. Results and discussion.....	54
3.5. CNC thin-film acoustic resonator modelling with FEM	62
3.6. CNC thin-film composite cantilever modelling with FEM	65
3.7. Conclusion	68
3.8. References	69
Chapter 4 – Ultrathin films of bacterial cellulose	71
4.1. Introduction	71
4.2. Materials and methods	73
4.3. Methods.....	74
4.4. Results and Discussion.....	77
4.4.1 Morphological analysis.....	77

4.4.2 Atomic Force Microscopy (AFM)	79
4.4.3 Fourier Transform Infrared Spectroscopy (FT-IR)	81
4.4.4 X-ray diffraction analysis (XRD)	84
4.4.5 Thermogravimetric analysis (TGA)	87
4.4.6 Differential Scanning Calorimetry (DSC)	89
4.4.7 Effect of alkaline treatment	90
4.4.8 Effect of ultrasound operating conditions	90
4.5. Conclusions	92
4.6. References	94
Chapter 5 – Summary of the new scientific results	97
5.1. Final closure	101
Vitae	102

Chapter 1

General introduction

Carbohydrates represent important structural and functional components of cells and tissues including simple sugars, starches, animal and plant celluloses, chitin, galactoglucosamins and many other compounds. They consist of three basic building blocks; single or double bonded oxygen, carbon and hydrogen in various conformations. The most basic carbohydrate units are monosaccharide, disaccharides and trisaccharides. Slightly higher polymeric degrees of carbohydrates are referred as oligosaccharides, while ten or more linked monosaccharide units are classified as polysaccharides^[1].

Monosaccharides can be further divided according to their carbon content as aldose, ketose, triose, tetrose, pentose, hexose or heptose. At this point it should be mentioned that biopolymers are generally divided into three major groups; polysaccharides, nucleic acids (DNA and RNA) and proteins, however the basic units can be similar. For example, pentoses (5-carbon monosaccharides) are the components of ribonucleic acid (RNA) and deoxyribonucleic acid (DNA), with de-oxylation of ribose at the second carbon in the later. In nucleic acid formation, the hydroxyl group of the first positioned carbon atom is replaced with a nucleotid base. Hexoses are stereoisomers (same molecular formula and sequence of atoms, but different three dimensional conformation), having identical stereo epimers and form subunits of celluloses and most sugars in fruits and blood. Epimers, chiral molecules can rotate the plane-polarized light for right (assigned as D) and left (assigned as L). Alfa (α) glycosidic bonds are formed between carbons having identical stereochemistry and beta (β) type glycosidic bonds are between different stereochemistry. D-glucose is a hexose repeating unit and principal component of cellulose via the β -1-4 glycosidic linkage. In xylan and chitin, amylose (α -1-4-linked), xylose and N-acetyl-D-glucosamin (β -1-4-linked) are known as homopolysaccharides. β -1-4 linked polysaccharides are known as structural integrity in organisms. α -1-4-linked amylose is an

energy-storage polysaccharide, denoted as a heteropolysaccharide since its repeating sugar unit consists of more than one type of sugar molecule.

In this way, a chemical characterization and basic units, main bonds within cellulose is built up. Cellulose is a most abundant natural biopolymer of linear β -1-4-linked glucose units at molecular level, which (in contrast to starch) are oriented with a CH_2OH group at C5. Cellulose can be found in higher plants, marine animal, algae, fungi, bacteria, invertebrates and even amoeba. The repeating unit is comprised of two anhydroglucose rings bond together in such a way that one molecule is rotated 180 degree in order to accommodate the bond angles of acetal oxygen bridges. Cellulose is fibrous, water insoluble substance and has a role in maintaining the structure of plant or marine animal cell walls. This fascinating biopolymer was first discovered and isolated by Anselme Payen in 1838^[2]. Frey-Wyssling et al. (1948)^[3] were the first to explore the plant cellulose fibrillar ultrastructure by electron microscopy. They found that essential and secondary cell walls exhibit a fibrillar texture. With respect to the molecular axis' terminal groups reducing functionality and a nonreducing end can be distinguished (Figure 1.1.).

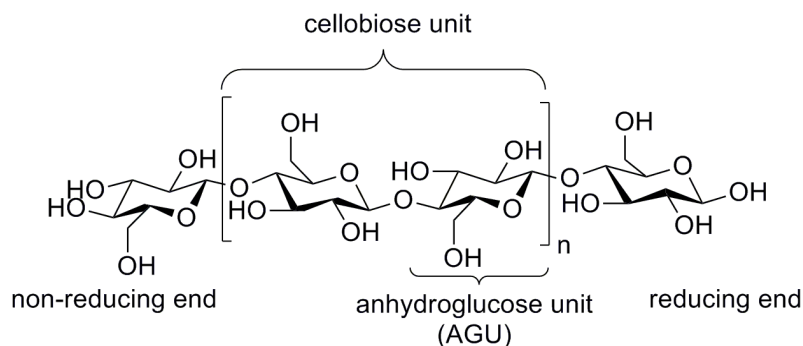


Figure 1.1. Molecular structure of cellulose

The glucopyranose rings have $4C_1$ chair conformations. Physical properties of cellulose are influenced by its supramolecular structure, namely the hydrogen bonding network. The three kinds of hydroxyl groups bond equatorially in anhydroglucose units under different polarities, and the resulting inter- and intramolecular interactions are responsible for the

stabilization, crystalline structure and hydrophilic nature of cellulose (Figure 1.2.). The H-s in the left ring serve as hydrogen bond donators, while O-s in the right ring including the glycosidic O bond contribute as hydrogen bond acceptors for the hydrogen bonding network (Figure 1.2.). In nature cellulose chain does not exist individually it is assembled of individual cellulose chains and forming fibrillary or fiber like material. In most of the higher plants cellulose is surrounded by hemicellulose and lignin matrix. Around 36 linear β -1-4-linked glucan chains form subfibrils (2-20 nm in diameter), which consist of repeating ordered (crystalline) and not ordered (amorphous or chain dislocations) parts in the fringed fibril theory. Pure cellulose subfibrils exist in bacterial cellulose and valonia only.

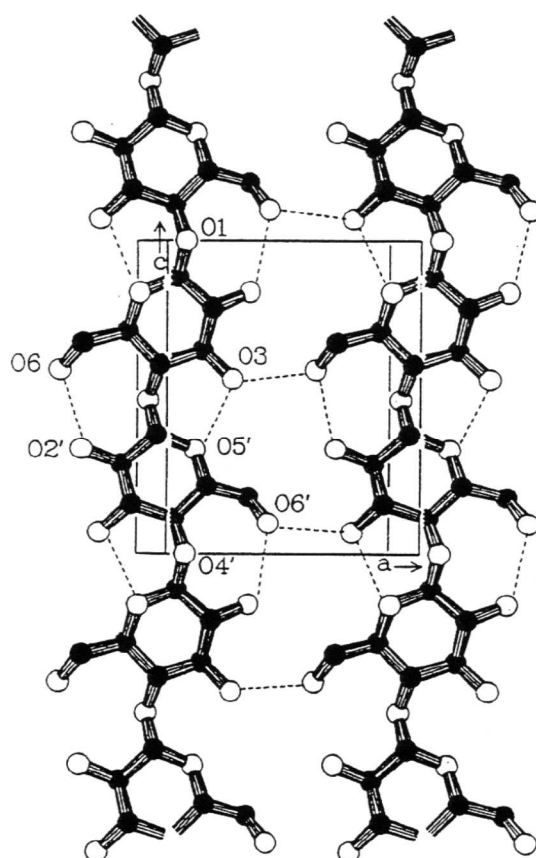


Figure 1.2. Most probable hydrogen bond pattern of cellulose I. (Kolpak and Blackwell 1976, 1978)

In the ordered cellulose chain region, strong and complex inter and intra molecular hydrogen-bond network formed. Hence cellulose subfibrils has different crystalline polymorphs. In native cellulose (cellulose I) found in nature, there are two intramolecular hydrogen bonds, which are between the OH-3...O5', and between the OH-2... O6' for bonding the layers and one intermolecular hydrogen bond, OH-6...O3 for linking the layers laterally, depending on the hydroxymethyl conformation at the C-6 position^[4].

Native cellulose I consists of two distinct crystal phases, namely $I\alpha$ and $I\beta$. The $I\alpha/I\beta$ ratio defines cellulose properties and varies within the cellulose microfibrils as well as in different cellulose sources. Algae and bacterial cellulose specimens are rich in $I\alpha$ form, while cotton, wood and ramie fibers are rich in $I\beta$ crystalline allomorph^[5].

The crystal structure and hydrogen-bonding system in cellulose $I\alpha$ and $I\beta$ respectively from synchrotron X-ray and neutron fiber diffraction apparatus are shown in Figure 1.3.

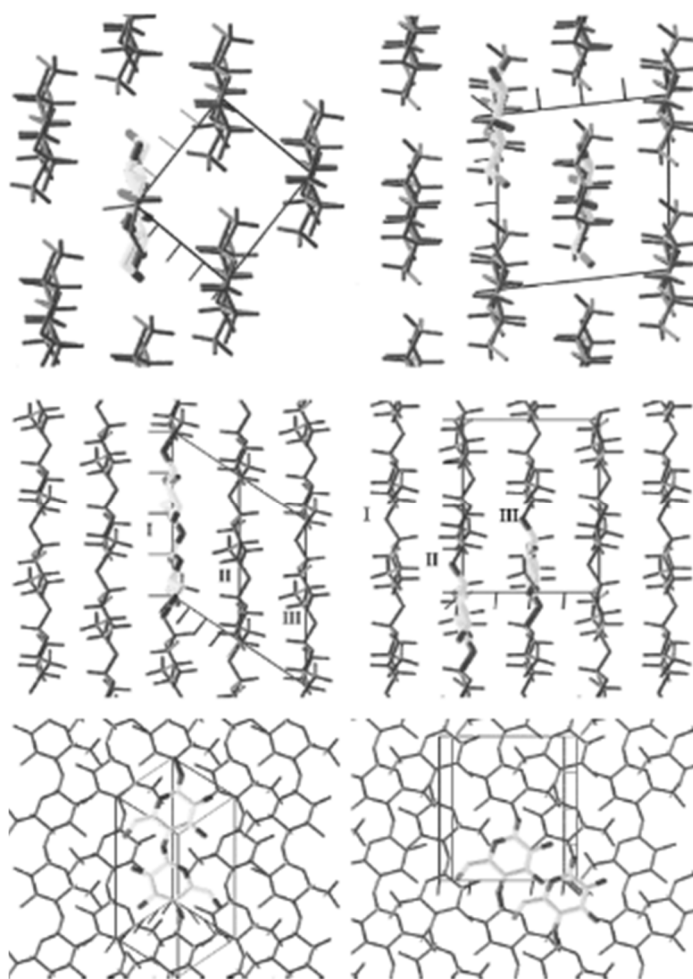


Figure 1.3. Crystal structures of cellulose $I\alpha$ (left) and $I\beta$ (right). Top row: down the chain axes. Middle row: perpendicular to the chain axis and in the plane of hydrogen bonded sheets. Bottom row: perpendicular to the hydrogen bonded sheets. ^[6]

In both of these structures, cellulose chains are parallel but they differ in their hydrogen bonding patterns, i.e. in the crystalline structure. $I\alpha$ corresponds to a triclinic unit cell ($a = 0.6717$ nm, $b = 0.5962$ nm, $c = 1.040$ nm, $\alpha = 118.080^\circ$, $\beta = 114.80^\circ$ and $\gamma = 80.37^\circ$) containing two chains per unit cell, while $I\beta$ exists in a monoclinic unit cell having one cellulose chain ($a = 0.7784$ nm, $b = 0.8201$ nm, $c = 1.038$ nm, $\alpha = \beta = 90^\circ$ and $\gamma = 96.5^\circ$). Furthermore, $I\alpha$ type cellulose is metastable and can be converted irreversibly into the irreversible $I\beta$. Later in the Chapter 2 the $I\alpha$ crystalline structure of cellulose has been used for the quantum mechanical polarization calculation, which has not been calculated in this context earlier.

Chemical, physical and enzymatic degradation of fibrillary cellulose fibers led to a colloidal suspension, which was observed by electron microscopy in 1950s as has been mentioned earlier. The observed degradation product was a needle-shaped crystalline cellulose particles having identical crystalline structure as the original fiber or fibrils. After the acid hydrolysis conditions were optimized, Marchessault et al.^[7] demonstrated that colloidal suspensions of cellulose nanocrystals (above a certain concentration) exhibited nematic liquid crystalline alignment, so the nanocrystals not randomly oriented in the liquid media. That observation helped later to explore the orientation of cellulose nanocrystals in thin films or surface functional modification. Chiral nematic alignment was one of the first natural film forming ability of CNCs colloid producing different colors under polarized light. The orientation of the CNCs is slightly different at each of the nematic planes due to rotation of the magnetic direction about the perpendicular cholesteric axis^[8]. Taking advantage of such phenomena, several techniques have been used in attempts to control the alignment of CNCs. These techniques include the rotational shearing of gels^[9] and the application of intense magnetic^[10,11] and electric fields^[12-14]. However, these techniques are time consuming and expensive, especially because the requirement of high (electric or magnetic) fields. Additionally, control over the thickness of the final films is not easily accomplished, nor the extension of the films. Most of these mentioned techniques resulted oriented cellulose nanocrystals on a drop size area only. A recent study of cellulose nanocrystal thin films demonstrated birefringence to be a result of intrinsic shape and optical anisotropy of rod-like cellulose nanocrystals, oriented by a spin-coating process. Birefringence varied with thickness and relative location to

the spin axis, allowing preparation of solid samples ordered for maximally anisotropy^[15].

Using the crude cellulase enzyme from *Trichoderma viride*, positive- and negative-type cellulose spherulites can be formed by artificial polymerization of cellulose via cellobiosyl fluoride, as observed by optical polarization microscopy^[16]. Like starch granules, spherules show optical birefringence, suggesting polymerization proceeds via two independent mechanisms. Under given polymerization conditions, the majority of the spherulites show a negative-type structure, indicating that cellulose chains within a spherulite have a predominantly tangential orientation^[17]. Both the introduced film formation techniques from cellulose nanocrystals and artificial polymerization of cellobiosyl fluoride resulted diverse applications in many scientific fields.

In general, the possibility to control the architecture of two- and three-dimensional arrays of proteins, nanoparticles and nanomaterials is critical in applications related to biotechnology (vaccines, diagnostics, etc.), biosensing, electronics, optics, microengineering and electrocatalysts^[17,18]. The same can be stated about the emerging utilization of CNCs as a building block for a broad range of structures, antimicrobial packaging and aerogels for wastewater treatment, drug delivery or surface coatings. In such cases the additional benefit of improved mechanical characteristics with aligned CNCs might be realized^[8]. Oriented cellulose nanocrystals offer potentially increased surface mechanical strength and wear resistance. A transverse Young's modulus, hardness and coefficient of friction of 8.3 ± 0.9 GPa, 0.38 ± 0.03 GPa and 0.51 ± 0.23 respectively, were determined. Notably, the transverse Young's modulus was found to be in agreement with reported values predicted by molecular modeling and measured for single CNCs by using atomic force microscopy, while the friction coefficient and wear resistance were enhanced and within the ranges that are useful in high performance applications^[19].

Cellulose nanocrystals have been used as a reinforcing material in composites to improve their mechanical properties^[20]. This is in part due to their relatively high intrinsic strength, high aspect ratio and low density. The use of CNCs in high performance coatings is attractive not only because of their expected properties but also because they may provide a platform for fundamental studies related to their assembly. When used in composites,

CNCs have been shown to affect markedly the properties of the resultant materials, depending on the processing conditions^[21] and their supramolecular organization^[18].

The overall aim of this chapter was to introduce and point the way forward of cellulose nanocrystal's characteristics, some basic processing and novel film-formation properties were also briefly outlined. The author feels that this basic knowledge is imperative to comprehend the overall importance of film forming ability and utilization of CNCs. For some readers there are obvious details, for others the entire Chapter might be unfamiliar. Nevertheless, this Introduction tried to summarize the essential features of cellulose nanocrystals with the hope that it is deep enough to provide valuable facts and information and short enough to avoid redundancies and tediousness. In the following sections further solutions are extended related to CNCs thin films, properties and applications by transforming them into a more formalized order, which attempts to address the following objectives:

- i) To develop of highly oriented cellulose nanocrystals and nanofibrillar films by calculating the dielectrophoretic and polarizability properties (electric field strength and frequency) using the Clausius-Mossotti approach.
- ii) To calculate the polarizability of the unit cellulose nanocrystal using quantum mechanical approach at subnanometer level.
- iii) To experimentally measure the piezoelectric response of the highly aligned cellulose nanocrystal thin films.
- iv) To develop and validate a finite element simulation (eigenfrequency analysis) of a piezoelectric cantilever.
- v) To fabricate bacterial cellulose nanofibrillar self-standing films for energy harvesting applications from bacterial cellulose.

The results of the theoretical, analytical and experimental works are presented in each chapter separately and are summarized in form of new scientific results at the end of the chapters.

Part of this general introduction chapter has been published by our research group in *Acta Histochemica* Vol. 115, pages 22-31, in 2013, in *Cellulose* Vol. 22, pages 779-788, in 2015, and in a Tappi Press published book chapter and some other journal listed in the references.

The potential benefits that can be gained through the formation of aligned CNC films are expected to broaden the possible applications of such sustainable, biologically-derived material. One of the most important emerging area of aligned cellulose nanocrystals or nanofibrils is in micro-energy harvesting systems. Energy harvesting systems made from cellulose is capable of scavenging milliwatts from solar, vibrational, thermal^[22] and biological sources. Our recently published works report micro-energy harvesting technologies, one based on vibrational piezoelectric^[23,24] system and the other one is based on solar energy^[25], which capable scavenging of $12 \mu\text{W}/\text{cm}^2$ energy in indoor environment.

1.1. References

1. J.F. Kennedy, C.A. White, In: Barton D, Ollis WD, Haslam E (eds) *Comprehensive organic chemistry*. Pergamon, Oxford 1979;5:755
2. Payen, A. *Compt. Rend.* 1838, 7, 1052.
3. A. Frey-Wyssling, K. Mühlethaler, R.G.W. Wyckoff, *Experientia* 4 (1948) 475-476.
4. T. Kondo, Chapter 3. Hydrogen bonds in cellulose and cellulose derivatives. *Polysaccharides: Structural diversity and functional versatility*. 1st edition, Marcel Dekker Inc., 2004, 69-98.
5. Y. Habibi, L.A. Lucia, O.J. Rojas, *Chemical Reviews*, 110 (6) (2010) 3479-3500.
6. Y. Nishiyama, J. Sugiyama, H. Chanzy, P. Langan, *J. Am. Chem. Soc.*, 125 (47) (2003) 14300-14306.
7. R. H. Marchessault, F.F. Morehead, N.M. Walter, *Nature*, 184 (1959) 632.
8. K. Fleming, D. G. Gray, S. Matthews, *Chemistry-a European Journal* 7, (9) (2001) 1831-1835.
9. N. Yoshiharu, K. Shigenori, W. Masahisa, O. Takeshi, *Macromolecules*, 30, (1997) 6395-6397.
10. J.F. Revol, L. Godbout, X.M. Dong, D.G. Gray, H. Chanzy, G. Maret, *Liq. Cryst.* 16 (1994) 127.
11. E.D. Cranston, D.G. Gray, *Science and Technology of Advanced Materials*, 7 (2006) 319-321.
12. Sugiyama, J.; Chanzy, H.; Maret, G., Orientation of cellulose microcrystals by strong magnetic-fields. *Macromolecules* 1992, 25, (16), 4232-4234.
13. D. Bordel, D. J.L. Putaux, L. Heux, *Langmuir*, 22, (11) (2006) 4899-4901.
14. Y. Habibi, T. Heim, R. Douillard, *Journal of Polymer Science Part B-Polymer Physics*, 46, (14) (2008) 1430-1436.
15. E.D. Cranston, D.G. Gray, *Colloids and Surfaces A: Physicochemical and Engineering Aspects* 325 (2008) 44-51.
16. S. Kobayashi, L.J. Hobson, J. Sakamoto, S. Kimura, J. Sugiyama, T. Imai, T. Itoh, *Biomacromolecules* 1(2000) 168-173.

17. W. Helbert, H. Chanzy, V. Planchot, A. Buleon, P. Colonna, *International Journal of Biological Macromolecules* 15 (1993) 183-187.
18. C. M. Niemeyer, *Angewandte Chemie-International Edition* 40, (22) (2001) 4128-4158.
19. Ingrid Hoeger, PhD, "Ultrathin Films of Cellulose and Lignin for Studies on Interfacial Phenomena". Supervisors: Orlando J. Rojas and Steve Kelley, NC State, 2011.
20. K. Oksman, A.P. Mathew, D. Bondeson, I. Kvien, *Composite Science and Technology*, 66 (2006) 2776–2784.
21. T. Ebeling, M. Paillet, R. Borsali, O. Diat, A. Dufresne, J. Y. Cavaille, H. Chanzy, *Langmuir* 15, (19) (1999) 6123-6126.
22. V. Nagy, I. Suleimanov, G. Molnár, L. Salmon, A. Bousseksou, L. Csoka, *J Mat Chem C* 3 (2015) 7897.
23. L. Csoka, I.C. Hoeger, O.J. Rojas, I. Peszlen, J.J. Pawlak, P.N. Peralta, *ACS Macro Letter* (2012), 867.
24. I.C Hoeger, L. Csoka, O.J. Rojas, *Assembly of CNC in Coatings for Mechanical, Piezoelectric and Biosensing Applications*. In: Michael T Postek, Robert J Moon, Alan W Rudie, Michael A Bilodeau (ed). *Production and Applications of Cellulose Nanomaterials*. Atlanta: TAPPI Press, 2013. pp. 71-74. (ISBN: 978-1-59510-224-9)
25. L. Csoka, D. Dudic, I. Petronijevic, C. Rozsa, K. Halasz, V. Djokovic, *Cellulose* 22 (2015) 779.

Chapter 2

Dielectrophoresis of cellulose nanocrystals**2.1. Introduction**

Ultrathin films of cellulose nanocrystals (CNCs) produced by controlled assembly have gained recent attention not only because of a number of emerging applications such as fabrication of advanced materials but also due to the fact that they can be used to better understand the nature of complex interactions in related systems.^[1-5]

Self-assembly of high aspect-ratio nanoparticles, such as CNCs, is facilitated by their geometry, dimensions, surface and intermolecular interaction forces and, from their response to external (electric and/or magnetic) fields. For example, convection-driven assembly has been used in coatings with spherical nano- and micro-particles.^[6,7] Highly crystalline CNCs obtained after their cleavage from the cell wall of fibers^[8-10] allows the creation of functional systems via simple and inexpensive self-assembly. Ultrathin films of cellulose nanocrystals (CNCs) have been developed by using the Langmuir-Schaeffer (LS) lifting^[11] and also the convective/shear assembly (CSA) techniques.^[12,13] The resulting structures were found to be isotropic in the case of the LS method, while the CSA films comprised aligned CNCs. In the latter approach, orientation was achieved by a subtle balance of effects that included nanoparticle geometry (aspect ratio, mainly), surface charge density of the CNCs and the substrate, surface tension forces and withdrawal rate in the CSA setup.^[12,13] Directed assembly of CNCs and microcrystals has been carried out using external electric,^[4,5,14-16] magnetic^[17-20] and shear fields.^[2,13,21] However, such external fields have had limited success in producing highly oriented CNCs within these films. Compared to magnetic fields, application of electric fields typically requires less energy. Furthermore, the fact that alternating current (AC) can be used opens additional opportunities for manipulation of particle orientation.

Shear alignment of CNCs in a convective assembly setup was shown to be an effective, inexpensive and scalable method.^[13] **However, improved control of orientation, faster processing and improved particle alignment, optimization are desirable. Therefore, we propose the fabrication of ultrathin films of highly oriented CNCs by using a convective/shear forces coupled with low intensity electric fields. Indeed, the second aim of this chapter was to present the polarization calculation based on quantum-mechanical approach.** In this respect, a classical molecular evaluation by dipole moments also included to get a better physical insight into such phenomena in an extended mode on cellulose nanocrystals.

Given the highlighted objectives, the first part of this chapter resulted one peer reviewed scientific publication in *Journal of Colloid and Interface Science* (a Q1 qualified journal), Vol. 363 in 2011, pages: 206-212 and three presentations at scientific symposia at 241st ACS Annual Conference, Los Angeles, CA, USA in 2011 and at 13th International Conference on Organized Molecular Films, Quebec City, Canada, July 18-21, in 2010 and at International Conference on Nanotechnology for the Forest Products Industry, Espoo, Finland, Tappi Press, in 2010, ISBN:9781618390011. The second part of that chapter has been worked out as an extension of the previous work using the quantum mechanical approach for the polarization calculation of cellulose nanocrystal.

2.2. Materials and methods

2.2.1 Materials

Ramie fibers from Stucken Melchers GmbH & Co., Germany, were used in the production of cellulose nanocrystals. The fibers were cut in small pieces and purified with a Soxhlet extraction system and then hydrolyzed with 65 % sulfuric acid at 55 °C for 30 min under continuous stirring. The resulting suspension was filtered through a sintered Buchner funnel, washed with deionized water and recovered by subsequent centrifugations at 10,000 rpm (10 °C) for 10 min each. Finally the resulting suspension was dialyzed against deionized water and then against Milli-Q water for a few weeks. The obtained CNC suspension was stored at 4 °C until use. The dimensions of the

CNCs were 185 ± 25 nm in length and 6.5 ± 0.7 nm in width, as determined by transmission electron microscopy^[22]. Deionized water from an ion-exchange system (Pureflow, Inc.) followed by treatment in a Milli-Q® Gradient unit with a resultant resistivity of >18 M Ω ·cm was used in all experiments. The particles were confirmed to be 88% crystalline as determined by WAXS. In theoretical consideration NFC (nano fibrillated cellulose) was also included in the calculation to see the effect of different dimensions of the particle up to 1000 nm.

2.2.2 Preparation of CNC films

Aqueous CNC suspensions of 2.5 wt% concentration were used in all particle deposition experiments by using a withdrawal speed of 8.4 cmh⁻¹, which was found to be optimal for obtaining highly oriented films^[12,13]. The CNC films were created in a convective assembly setup combined with an AC electric field. The AC electric field was generated by a power amplifier (Krohn-Hite Model 7500-DC to 1 MHz wideband power amplifier, Krohn-Hite Corp., Brockton, MA) driven by a sine wave from a function generator (Wavetek Model 134, Wavetek Corp., San Diego, CA). The reported voltages are peak-to-peak values.

Microscope glass slides were used as support for thin sheets of freshly cleaved mica which were used as a carrier of the CNC film. To this end mica sheets were gently glued onto the glass slides and the topmost layer was peeled off to uncover a clean, pristine mica surface. Before CNC assembly, the glass-mica carrier was treated with a 500 ppm polyethyleneimine (PEI) solution, which made cationic charges available for electrostatic interactions with the negatively charged CNCs. In the course of convective self-assembly, a droplet (ca. 20 μ l) of liquid suspension was placed in the wedge formed by a tilted (24°) glass slide and the mica carrier (Figure 2.1). The CNC suspension was held by capillary forces and the liquid meniscus was withdrawn horizontally across the mica carrier by translating the tilted glass slide. This translation was produced with a syringe pump (NE-500 New era pump systems, Inc, Wantagh, NY) that moved the tilted glass at a constant speed of 8.4 cmh⁻¹. To create the constant AC electric field around the mica carrier, two parallel aluminum electrodes spaced 5 mm apart from each other were placed on the edges of the mica sheet and connected to a power amplifier

(see Figure 2.1). The CNC film deposition was carried out at room humidity and temperature.

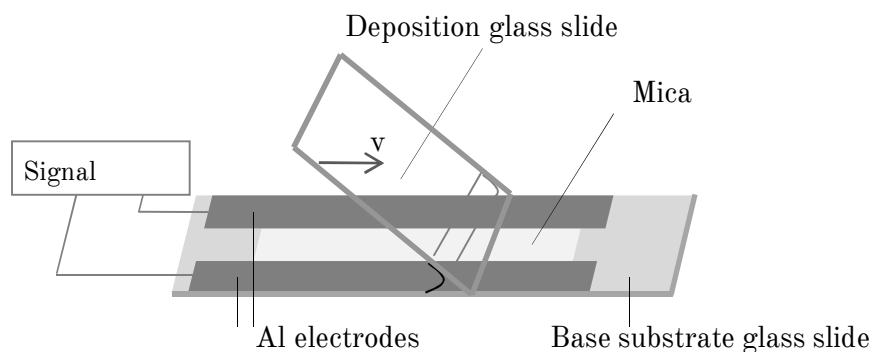


Figure 2.1. Schematic illustration of the convective assembly setup coupled with an electric field. In a typical experiment, a volume of CNC suspension was placed between a tilted, deposition glass slide and a base substrate consisting of mica with pre-adsorbed PEI (polyethyleneimine) and supported on a glass slide. The distance between the aluminum electrodes was 5 mm and withdrawal of the deposition glass slide occurred in the horizontal direction at a constant speed (v) of 8.4 cmh⁻¹

The system was driven by a computer, allowing precise control of the withdrawal speed. The alignment of CNCs in the obtained ultrathin films with application of AC electric fields was examined at field strengths of 100, 400 and 800 Vcm⁻¹ and frequencies of 200 and 2000 Hz. The results were compared against assemblies obtained in the absence of external electric fields. The typical thicknesses of the deposited films were ca. 38 nm, as measured by ellipsometry.

A Matlab code was used to determine the degree of CNC alignment. AFM height images were used to perform grain partition and filtering and the resulting images were analyzed for the angles of the long axis of the CNCs with respect to a reference line in the withdrawal direction. The degree of CNC alignment was defined as the number % of CNCs in the angle range between 0 and 20 degrees in the withdrawal direction considering symmetry conditions. Typically, more than 300 CNCs were counted in image processing and at least 3 different locations, from the different films were

analyzed for each condition. More details about this method can be found in Ref. ^[13].

An AFM XE 100 from Park Systems (Santa Clara, CA) was used in non-contact mode to obtain topographic images of the surface. A pyramidal silicon tip with a radius of less than 10 nm and an aluminum coating on the backside (Park Systems, Santa Clara, CA) was used with an applied constant force of 42 Nm⁻¹ and a frequency of 330 KHz. At least three different films at three different positions were imaged for each deposition condition used. The images were analyzed using the XEI software, and only flattening of one regression order was used to correct the slope of the tip/sample interaction.

To apply a style, begin by selecting the text to which the style needs to be applied, and then choose the style name from the styles list box on the tool bar or by using WSPC Toolbar. The WSPC templates contain all the styles that are required for formatting the documents. It is crucial and recommended to exploit the usage of styles as much as possible to format the text. However, apply direct formatting only as a last resort when the style, for some reason, is incompatible with the requisite. As a note of caution, do not use any style for a purpose other than that for which it was intended or for the want of effort.

2.3. Theoretical consideration

Frequency-dependent changes in polarizability of biological cells and colloidal particles^[23] take place from structural, Maxwell-Wagner polarization effects.^[24-26] Dielectric models have considered the properties of the particles by assuming spherical or ellipsoidal geometries.^[27,28] When colloidal particles are suspended in low conductivity medium different states of polarizability occur, less or more polarizable than the medium. These states of polarizability are frequency-dependent. At low frequencies the surface charges are expected not to affect the polarization mechanism while at high frequencies the differences in permittivity are dominant factors.^[29] The charges of opposite signs on either side of the particle lead to an effective net-induced dipole moment. In dielectrophoresis (DEP), when a non-uniform electric field is applied on a dielectric particle, a force unbalance takes place, as described by Pohl in 1951.^[30] Consequently the colloidal particles move

towards or away from regions of high field, depending on their polarizability relative to that of the medium.^[31,32]

Similar phenomenology as the one described above is expected to offer a simple approach to align CNCs at low AC electric fields. Calculated dipole moments and the Clausius-Mossotti factors can describe the critical frequencies for alignment and the peak dielectrophoresis of CNCs. The DEP is a phenomenon where a force is exerted on a dielectric particle in a non-uniform electric field to move or rotate it in a given surrounding media. The potential at the crystal surface depends on the field frequency as well as electrical and geometrical characteristics. In this investigation a prolate spheroid geometry was assumed for the CNCs.^[33,34] It was also assumed that during polarization by an external, homogeneous electric field the ellipsoid CNCs acquired only a dipolar moment; multipoles of higher orders were assumed to be absent.^[35]

The dipole moment depends on the frequency of the applied electric field and the dielectric properties (permittivity and conductivity) of the particle and the fluid.^[36]

The dielectric force F_{DEP} can be described by

$$F_{DEP} = p_1 \nabla E_0 \quad (2.1)$$

where E_0 is the applied electric field and p_1 is the dipole moment. The dipole moment for an ellipsoid can be calculated by the volume integral of the polarization vector (\overline{P}), which is constant over the volume:

$$p_i = 4\pi a^2 b \overline{\varepsilon_m} K_i E_i \quad (2.2)$$

where a, b stand for the major and minor half axes, respectively and the $i = x, y$ components represents the directions projected along these axes of the particle. ε is the permittivity of the medium and K_i denote the Clausius-Mossotti (CM) factor. The complex CM factor for homogeneous ellipsoid can be written as:

$$K_i(\omega) = \frac{1}{3} \frac{(\bar{\epsilon}_p - \bar{\epsilon}_m)}{\bar{\epsilon}_m + A_i(\bar{\epsilon}_p - \bar{\epsilon}_m)} \quad (2.3)$$

with

$$\bar{\epsilon} = \epsilon - i \frac{\sigma}{\epsilon_0 \omega} \quad (2.4)$$

where p and m refer to the particle and the medium, respectively. σ is the conductivity of the dielectric and ω is the angular frequency of the applied field. A_i is a component of the depolarization factor along any of the three axes of the ellipsoid ($i=1, 2, 3$). For a prolate ellipsoid the major axis component of the depolarization factor is given by

$$A_x = \frac{1-e^2}{2e^2} \left[\log\left(\frac{1+e}{1-e}\right) - 2e \right] \quad (2.5)$$

where e is the eccentricity:

$$e = \sqrt{1 - \left(\frac{b}{a}\right)^2} \quad (2.6)$$

If the particle shape is close to spherical, e tends to unity, as expected. Due to the symmetry of the ellipsoid of revolution, the components of the depolarization factor at the two other axes of the prolate ellipsoid ($i=y, z$) have the same value, given as:

$$A_z = A_y = \frac{1-A_x}{2} \quad (2.7)$$

Finally, the DEP behavior can be described using the average of the real part of the Clausius-Mossotti factor for the three possible axes of polarization:

$$\operatorname{Re}[K(\omega)] = \frac{1}{3} \sum_{i=x,y,z} \operatorname{Re}[K_i(\omega)] \quad (2.8)$$

On the other hand, the rotation of particles can be determined by the equilibrium of hydrodynamic and electrorotation (ER) torque, according to the imaginary part of the Clausius-Mossotti factor:

$$\operatorname{Im}[K(\omega)] = \frac{1}{3} \sum_{i=x,y,z} \operatorname{Im}[K_i(\omega)] \quad (2.9)$$

The nature of the particle or the type of material is critical. Of relevance to the present work are the measured dielectric properties of cellulose: cellulose,^[37] cellophane,^[38] microcrystalline cellulose^[39] and regenerated cellulose,^[40] which have been reported to be similar (values below 0.1 MHz). In this work the real and imaginary part of the CM factor were calculated by assuming the dielectric constants (permittivity and conductivity at given frequencies) and provided in Ref. ^[40]

Figure 2.2 shows the real and imaginary components of the CM factor for CNCs calculated at different temperatures. Since the polarizability of CNCs is low (see Figure 2.2(a) for the real part of the Clausius-Mossotti factor), $\operatorname{Re}[K_i(\omega)]$ becomes negative ($\operatorname{Re}[K_i(\omega)] < 0$), and the particles are expected to move toward regions with minimum electric fields. This is called negative dielectrophoresis (n-DEP). As the water medium temperature increases the real part of the CM factor is shifted to higher frequencies but still remains in the negative dielectrophoresis (n-DEP) region. At high frequencies (beyond 10^3 Hz), the value of the real part of the Clausius-Mossotti factor changes sharply but remains in the n-DEP region. As can be observed in Figure 2.2(a), the calculated real part of the CM factor have no crossover frequency; this was also the case when different medium conductivities were considered.

From Fig. 2.2b, we can assume that a frequency of the electrical field around 2 kHz can be useful for the CFCs alignment during the shear assembly.

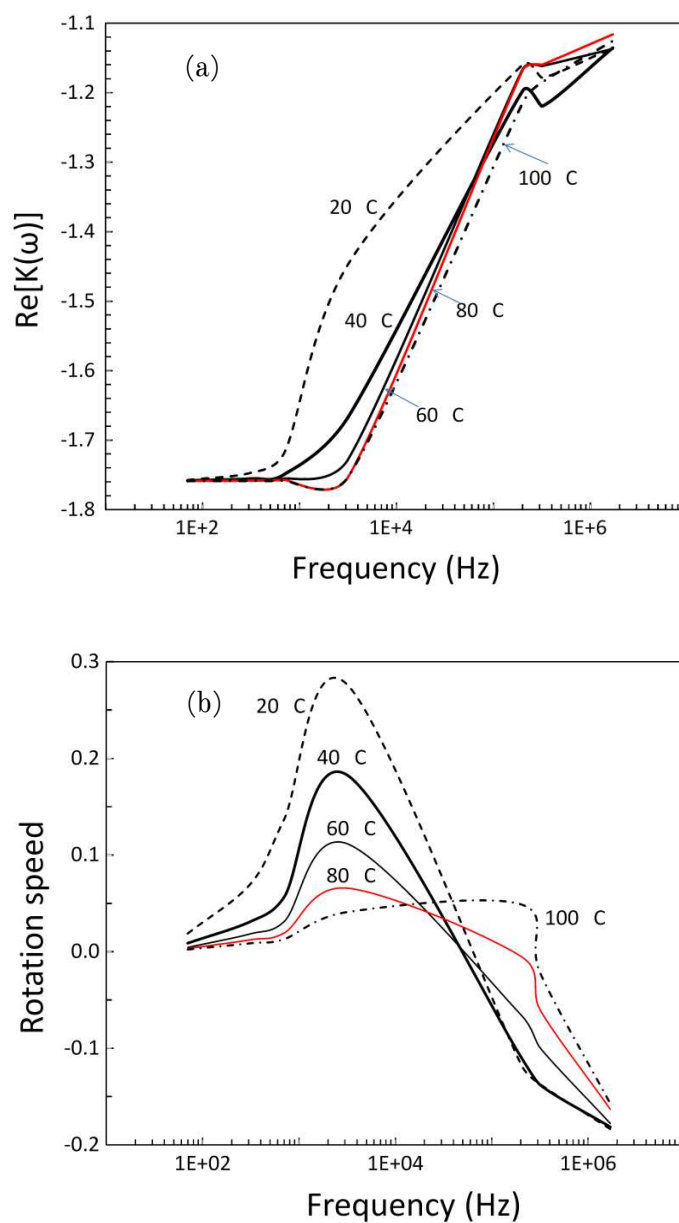


Figure 2.2. Real (a) and imaginary (b) components of the Clausius-Mossotti factor as a function of the frequency of the electric field applied to CNCs. The CNCs were modeled as prolate ellipsoids and suspended in aqueous medium.

The b/a ratio was found to play a minor role in nanoparticle rotation rates, changes by no more than tenths of a percent were calculated. This result is explained by the fact that the reduction in the moment of electrical forces (polarization in the direction normal to the symmetry axis decreases for elongated ellipsoids) is compensated by a diminishing viscous friction.^[26,41]

In the 20-100 °C temperature range the peaks of the electro-rotation (ER) spectrum of CNCs shifted linearly to higher frequencies with T (see Figure 2.2(b)). This is due to the inverse temperature dependence of permittivity and conductivity. When the temperature is increased, the intermolecular forces become less dominant and the particles are more unrestricted to respond to the applied electric field, thus giving a shifted peak at higher field frequency. A temperature of 25 °C was used in further theoretical and experimental considerations (no significant changes with temperature of the medium were observed).

Fig. 2.3 shows the real and imaginary components of the Clausius-Mossotti (CM) factor for NFCs calculated at different lengths. Since the polarizability of NFCs is low, same as CNCs (see Fig. 2.3a for the real part of the Clausius-Mossotti factor), $\text{Re}[K_i(\omega)]$ becomes negative ($\text{Re}[K_i(\omega)] < 0$), and the particles are expected to move toward regions with minimum electric fields similar to CNCs. As the length of NFCs increases (the diameter stay 20 nm for each), the real part of the CM factor is shifted to higher frequencies but still remains in the negative dielectrophoresis (n-DEP) region. At high frequencies (beyond 700 Hz), the value of the real part of the Clausius-Mossotti factor changes sharply but remains in the n-DEP region. As can be observed in Fig. 3a, the calculated real part of the CM factor have no crossover frequency.

In the 200–1000 nm length range, the peaks of the electrorotation (ER) spectrum of NFCs shifted linearly to lower frequencies with length (see Fig. 3b). But the magnitude of the rotation speed is increased compare to CNCs.

From Fig. 2.3b, we can assume that a frequency of the electrical field between 700-1000 Hz can be useful for the NFCs alignment during the shear assembly, which is roughly the half than can be used for CNCs.

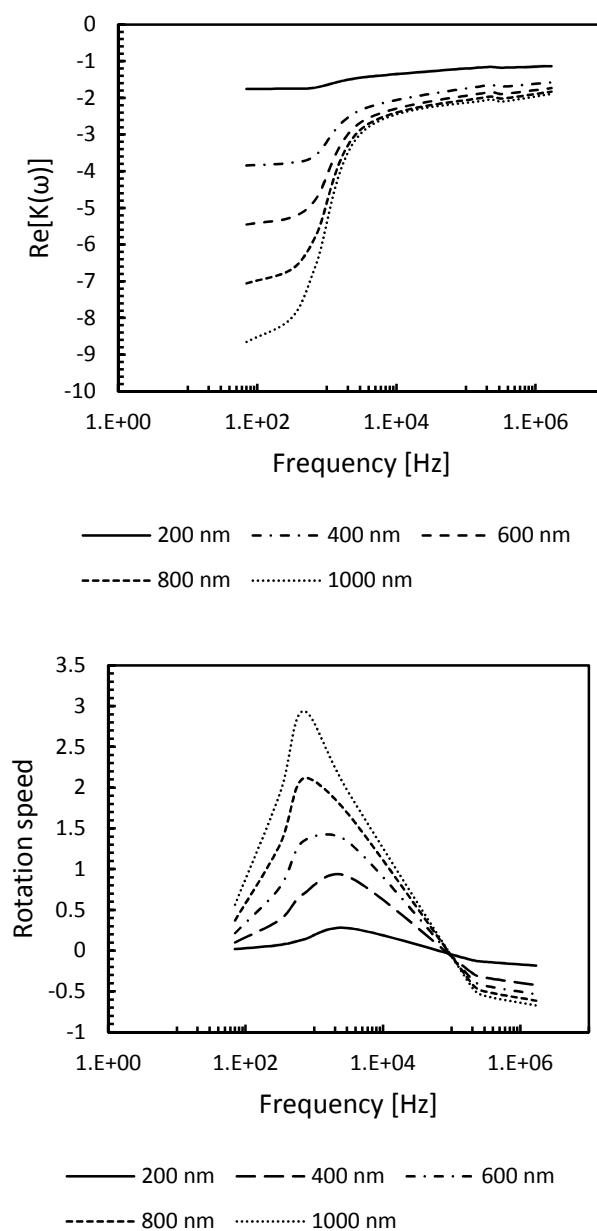


Figure 2.3. Real (a) and imaginary (b) components of the Clausius-Mossotti factor as a function of the frequency of the electric field applied to NFCs.

In sum, the calculated polarizability of prolate objects in aqueous solution was used to describe electrophoretic phenomena of CNCs and NFCs subjected to electric fields. Resulting CM spectra for dielectric properties of homogeneous prolate ellipsoids assisted in discriminating between purely physical and temperature-induced changes,^[27] and to find the optimal field strength and frequency for isotropic alignment. The polarization model introduced here was further used to understand and control the alignment of CNCs during film formation. Results for CNC alignment in ultrathin films are described in more detail in the next section in light of the CM function. NFCs were used only in the theoretical approach showing the CM function at different length of the particle.

2.4. Results and discussion

Ultrathin films of CNCs deposited on mica surfaces were observed in air by using AFM. In our earlier work CNC suspension subjected to shear/convective forces was shown to produce a disorder film on mica. Other substrates were found to favor better alignment under the experimental conditions employed. Therefore, mica as the most unfavorable substrate for CNC alignment was used in this work. This condition also helps in decoupling the effects of electric field from the complex contributions of shear and capillary forces.^[13] Prior to AC field-assisted shear assembly, two reference deposition experiments, without application of electric fields, were carried out. AFM images of ultrathin film of CNCs assembled on mica and also on mica with a pre-adsorbed layer of PEI are presented in Figures 2.4a and 2.4b, respectively.

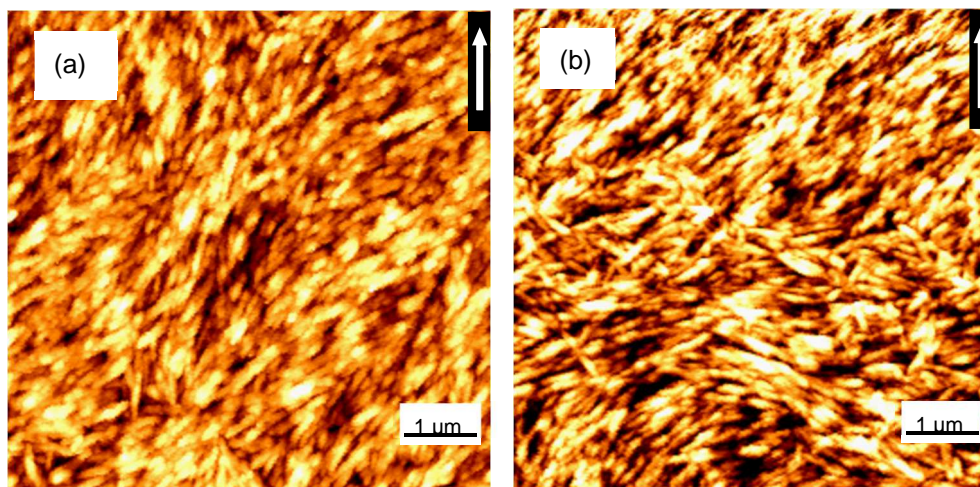


Figure 2.4. CNC films assembled on pure mica (a) and on mica with a pre-adsorbed layer of cationic PEI (b) by the CSA technique. The withdrawal direction is indicated by the arrow. The films were produced with the AC electric field turned off.

The withdrawal direction is indicated in these figures by the respective vector which was used relative at a given angle of the applied electric field. It can be generally concluded that shear forces created randomly oriented, anisotropic multilayers of CNCs.^[13] The degree of alignment quantified by

the number density of CNCs in the angle range between 0 and $\pm 20^\circ$ on pure mica (Figure 2.4a) and on mica with a pre-adsorbed layer of PEI (Figure 4b), was 16 and 56%, respectively. It was noted that the data for the experimental degree of alignment had a large standard deviation owing to the disordered nature of the film.

Film formation was observed to depend on the withdrawal speed (see Experimental section) and on the rate of solvent evaporation. Mica was primed with a pre-adsorbed layer of cationic PEI, with an ellipsometric thickness of less than 1 nm. The films of CNC deposited on the mica pre-treated with PEI were multilayered, as can be determined from typical CNC film thicknesses of ca. 40 nm. More homogeneous deposition was favored in the case of the positively charged substrate. The bottom layer of CNCs was expected to bind to PEI via van der Waals and electrostatic interactions, rather than by forming crosslinked networks.^[42] Such anchored layer likely worked as an insulation and under an AC electric field it facilitated alignment of CNCs in the upper layers. In fact, the PEI adsorbed layer was shown to facilitate a linear growth of ultrathin films of CNCs.

During deposition, the withdrawal speed must be matched with that of the settling particles so as to maintain a continuous and homogeneous film consolidation. Moreover, the deposition surface must be wetted by the CNC suspension in order to enable sliding on the substrate, to maintain a constant evaporation rate and to form a stable film.^[43] At high evaporation rates instabilities in the growth of the structure, for example rupture or stripping of the film, may occur.^[44]

In the experiments the evaporation rate decreased linearly with time and therefore the formation of structured assemblies improved after some withdrawal distance from the initiation of the deposition, i.e., at a distance from the edge of the deposited film of CNCs.

In contrast to the randomly oriented CNC film shown in Figure 2.4, application of an external electric field induced CNC orientation. For example, Figure 2.5 shows aligned nanoparticles on mica with pre-adsorbed PEI in films obtained by shear assembly coupled with an electric field of 100 Vcm^{-1} AC and 2 kHz frequency.

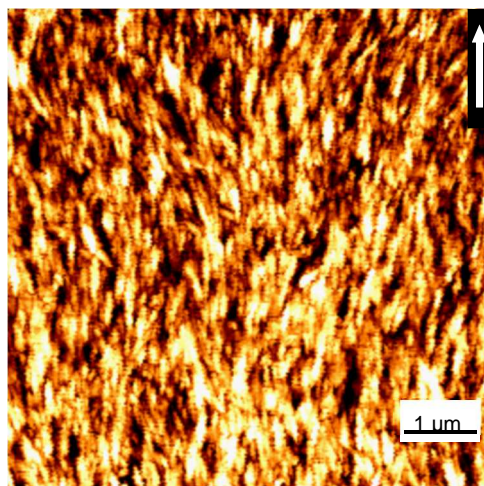


Figure 2.5. AFM height image of an ultrathin film of CNCs assembled under an electric field of 100 Vcm^{-1} and 2 kHz frequency. The electric field vector is perpendicular to the withdrawal direction, which is indicated by the arrow.

In the experiments illustrated in Figure 2.5 the electric field was directed perpendicular to the withdrawal direction. However, by changing the field strength and frequency the orientation direction could be altered according to the bivariate map for the orientation parameter (O_p) shown in Figure 2.6. In this figure the polarizability of CNCs is presented as a function of field strength and frequency.

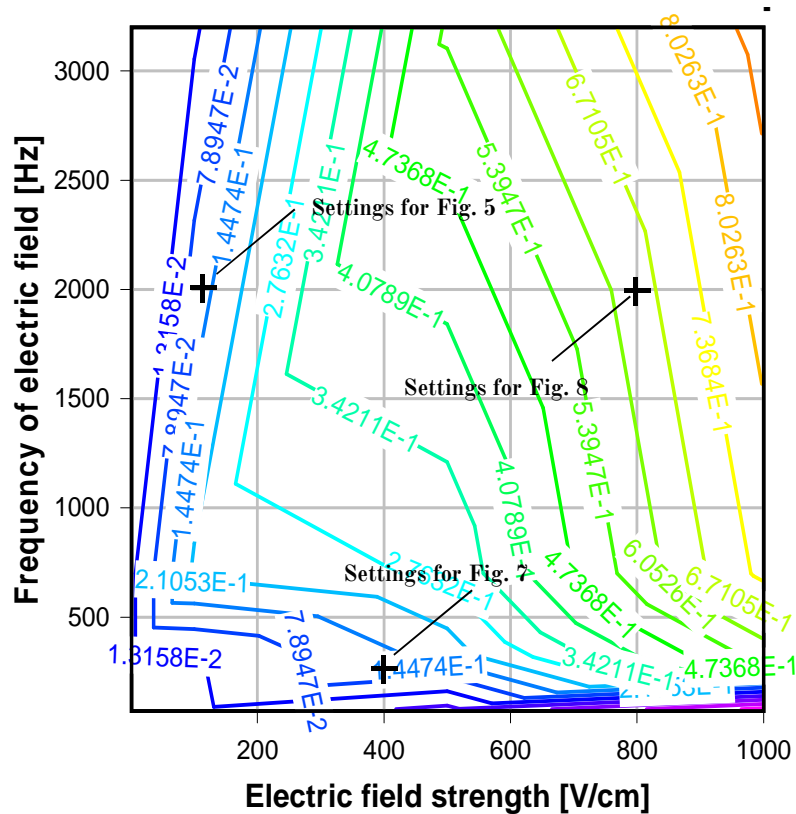


Figure 2.6. Magnitude of the orientation parameter (O_p) of CNCs as a function of field strength and frequency. This bivariate map was plotted using DPlot Graph software, according to the equations described in the text. Crosses are drawn at frequency-field strength conditions used in experiments that yielded films illustrated in Figures 2.5, 2.7 and 2.8.

The effective polarizability is the proportionality constant in the linear relationship between the induced dipole moment and the external field. More specifically, dipoles and particles such as CNCs have a special form of polarization, on account of the Maxwell-Boltzmann distribution (MBd); the dipoles can be oriented in such a way to have a net dipole moment along the direction of the field.

The component of the external electric field direction of the dipole moment can be calculated from Eq. 2.10:

$$-p_i \cos \theta \quad (2.10)$$

and the potential energy of a dipole in an electric field can be calculated as the real part of the scalar product in Eq. 2.11:

$$V(\theta) = -A\Re(p \cdot E) \quad (2.11)$$

where A is a factor that can be used to adjust the theoretical model to the numerical data and θ is the angle between the dipole axis of the particle and the direction of electric field.^[45]

If all orientations in water medium were equally likely, the average component along the field would be zero.^[45] But on account of the MBd, the probability (P) of finding the dipole axis is proportional to:^[46]

$$P_{MBd} = \frac{e^{-\frac{V(\theta)}{kT}}}{\int_0^{\pi/2} e^{-\frac{V(\theta)}{kT}} d\theta} \quad (2.12)$$

where k is the Boltzman's constant, and T the temperature. Hence, the orientation parameter (O_p) can be calculated by integration of the MBd over solid angles:

$$O_p = \int_0^{\pi/2} P_{MBd} \cos 2\theta d\theta \quad (2.13)$$

This function (Eq. 2.13) is proportional to the external field in the bivariate plot shown in Figure 2.5. It can be seen that at low field strength and frequency the mean dipole moment is proportional to the field and the polarizability and the dipoles are oriented antiparallel to the electric field, as was the case observed in Figure 2.7. Over the inflection point (at a value of

O_p of 0.407, Fig. 2.6) high field saturation starts to take place and all the dipoles are parallel to the external field.

At low-frequency AC fields, particle polarization and interactions are controlled by the particle and fluid conductivities.^[47] This effect is frequency-dependent in the case of cellulose in aqueous medium.^[40] At high-frequency AC fields, the charges have insufficient time to respond and orientation polarization is dominant; conductivity no longer plays a role.^[48-50] In the present case of low-to-medium frequencies, both the permittivity and conductivity are important.

In order to further illustrate the implications of the bivariate map shown in Figure 2.6, a series of experiments were conducted to validate the predictions for the direction and degree of alignment. Moreover, image analyses were performed on AFM scans using a MATLAB code to calculate the alignment of CNC particles according to O_p (reported here as % number density of particles in the $0 - \pm 20^\circ$ leading angle range). The alignment of CNC particles at low intensity electric field and frequency (400 Vcm^{-1} and 200 Hz) was 46 %; at low intensity electric field and high frequency (100 Vcm^{-1} and 2000 Hz) it was 77 %. At high intensity electric field and frequency (800 Vcm^{-1} and 2000 Hz) it was 88 %. The combination of electric fields and shear forces that favored alignment in the same direction produced nearly perfect orientation of CNCs in the film.

Figure 2.7 shows an AFM scan of the end section of a CNC film deposited on mica with pre-adsorbed PEI and obtained by shear assembly assisted with an electric field of 400 Vcm^{-1} AC and 200 Hz frequency. In this arrangement anisotropy and some degree of alignment was observed in the section close to the edge. For this field strength and frequency range the particles were expected to align perpendicular to the electric field (see bivariate map in Figure 2.6).

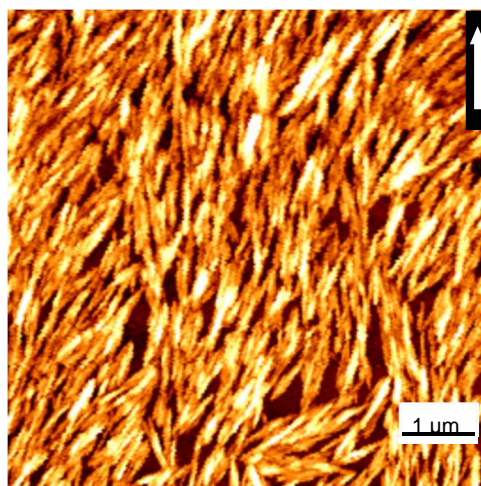


Figure 2.7. AFM height image end sections of ultrathin film of CNCs formed under an electric field of 400 V cm^{-1} and 200 Hz. The preferred alignment is parallel to the withdrawal direction, indicated by the arrow. The length of the deposited CNCs film on mica with pre-adsorbed PEI was 5 cm.

In contrast, when the electric field strength and frequency were increased, the CNCs tended to align parallel to the field direction, as shown in Figure 2.8. Highly oriented, anisotropic structures were observed in the middle section of the film.

If simultaneously the AC electric field and frequency are decreased, the magnitude of the induced dipole moment of the CNCs also decreases and the field-induced rotational torque is not large enough to overcome thermal forces. Consequently, the isotropic phase grows and eventually spans the entire frequency range.^[51]

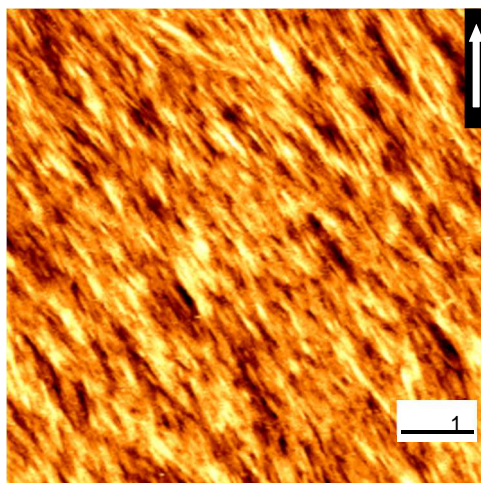


Figure 2.8. AFM height image of the middle sections of ultrathin film of CNCs formed under an electric field of 800 Vcm^{-1} and 2000 Hz. The alignment of particles produced a highly oriented structure. The electric field vector in this case is perpendicular to the withdrawal direction, indicated by the arrow.

It was observed that over large scanned areas the ultrathin films of CNCs exhibited ordered and disordered domains. This can be explained by the polydispersity of the particle suspension or nanocrystal aggregates which created instabilities in the alignment, during film deposition. Different particle geometries can also cause some dislocations or multilayer formation. However, the developed technique for ultrathin film coating showed that the process of alignment was stable for the middle part of the film and that dislocations were damped with the progress of film deposition (steady state conditions) and also by the decreasing CNC volume fraction as solvent evaporation occurs (in the meniscus formed between the substrate and the moving plate, see Experimental).

The effect of geometry and size of CNCs are expected to be relevant. Such variables may affect water evaporation rate and explain the inhomogeneous volume fraction during the shear assembly and also the formation of aggregates after deposition. In order to obtain a more direct understanding of such effects, further experiments with CNCs of different average size and size distributions must be performed.

The main parameters that affect the formation of ultrathin films are accounted in Dimitrov and Nagayama equation:^[43]

$$v_c = \frac{\beta l j_e \varphi}{h(1-\xi)(1-\varphi)} \quad (2.14)$$

where ξ and h are the porosity and height of the deposited colloidal crystal, φ is the volume fraction of the particles in suspensions, j_e is the evaporation flux, and l is the evaporation length (which is the integral of total evaporation flux per unit length). β is an interaction parameter that relates to the mean solvent velocity to the mean particle speed before entering the drying domain^[52] and takes values between 0 and 1. β depends on the particle-particle and particle-substrate interaction: the stronger the interaction, the smaller β will be. PEI treatment of mica decreased β relative to the value for bare mica. It can be concluded that reducing the withdrawal speed may increase the alignment further, as calculated for the evaporation length by using 0.74 for the density of packed ellipsoids and considering that water evaporation flux per unit length did not depend on the particle diameter ($l \approx 4.2$ cm for 8.4 cmh⁻¹).

Deposition speed exceeding the natural assembly rate of a monolayer, as described by Eq. 2.14, results in incompletely ordered films.^[53] If the ambient air around the deposition plate is not saturated by water vapor, fast, ordered assembly is expected to take place under electric fields (Fig. 2.8).

The primary driving force for the convective transfer of CNC particles is the water evaporation from the freshly formed aligned CNC film. The volume of the CNC suspension decreases with the withdrawal motion and the film thins out gradually, as the water evaporates. Unsaturated air with water vapor around the forming film causes influx from the meniscus toward the formed film. This influx compensates the evaporation of water from the film and particle flux makes a dense, aligned CNC film under the electric field. The particle flux is obviously stronger than the migration effect of low voltage electric field and, as stated, CNCs are subject to negative dielectrophoresis (the particles tend to align at low electric fields). Because the AC voltage is maintained in the entire withdrawal shear process, until the water is evaporated, the densely packed alignment cannot change further.

The model handles simultaneously the dielectric properties of CNCs and water medium around it. When water evaporates to unsaturated ambient air, the ratio between the dielectric materials will change. Hence the formation of the aligned CNC film is irreversible when the proper amount of water evaporates.

Using the theoretical consideration above (eq.2.1-2.9) a finite element model has been built up to effectively simulate the dielectrophoretic behavior of CNCs on a lab-on-a-chip device. With that dielectrophoretic approach the CNC particles can be sorted, separated and also control the film formation. In the following section we demonstrate the fabrication of periodic and alternate, short particles using n-DEP. The Clausius-Mossotti principle behind is schematically depicted in Fig. 2.9.

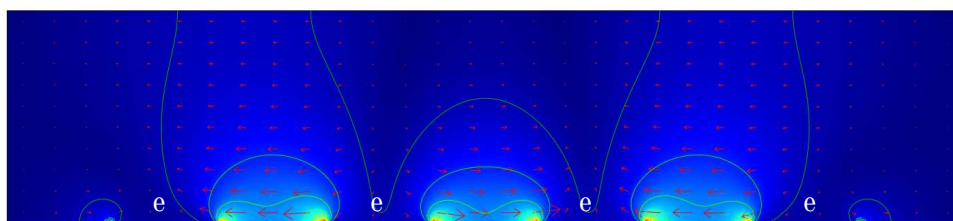


Figure 2.9. Principle of shorting CNCs with a microfluidic device. A cross sectional view of the electrical field strength formed around the electrodes (e). Bright areas corresponding to higher electric field appear at both edges and surfaces of the electrodes.

An integrated array electrode with four independent microelectrode subunits ($200\ \mu\text{m}$ wide and $\sim 100\ \mu\text{m}$ distance between them) was fabricated as a template to short CNCs. In the present system, the n-DEP force is induced by applying an AC voltage and frequency (optimized above) to align CNCs toward a weaker region of electric field strength. These regions are indicated by light blue between the electrodes at the bottom of the image (Fig.2.9.). The CNCs were guided apart from the high electric field regions (from the edges of the electrodes and from their surface). Dielectrophoretic patterning was observed under a AFM microscope after drying the patterned CNC film.

The following 2 images (Fig.2.10. a and b) show the built n-DEP type chip device with the CNC suspension on it (Fig.2.10.b).

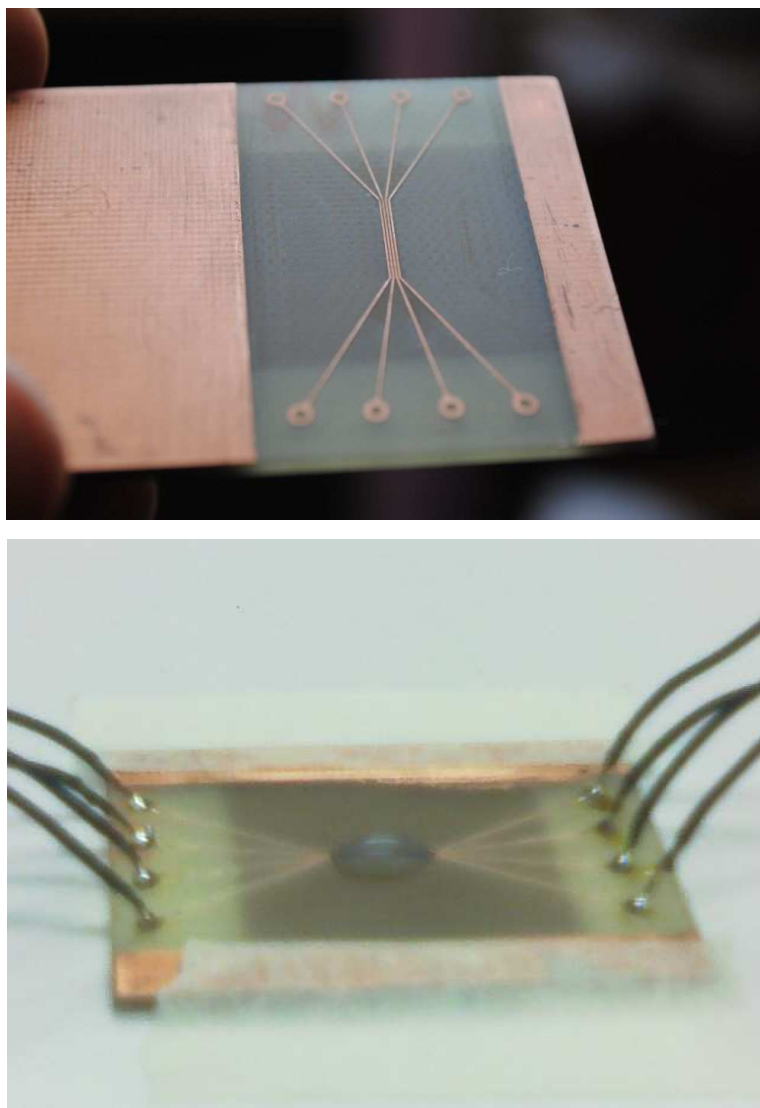


Figure 2.10: a and b. A modeled microfluidic device after fabrication (a) and with CNC suspension and AC connections.

The strength of the AC electric field was visualized using Comsol Multiphysics finite element software package. Fig. 2.9 clearly shows that deep valleys of electric fields are created above the electrodes and high mountains between the bands. Thus, suspended CNC particles moved to that areas (between the bands) in the n-DEP electrical and frequency region. When the water evaporated the low electric field regions was observed by AFM microscopy. It can be clearly seen in Fig. 2.11. that the n-DEP region of the device were loaded with aligned CNCs.

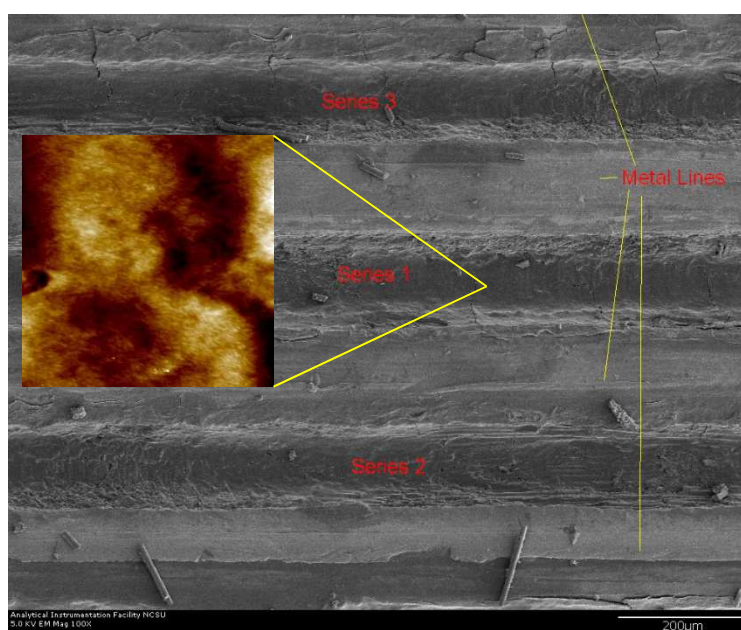


Figure 2.11. AFM image about the patterned CNCs between the electrodes.

In sum, the polarizability of CNCs has been considered in an electric field, and used to interpret CNC alignment in a convective assembly setup that induced shear forces during withdrawal of the deposition plate. While this is clearly an approximation to describe the highly complex system involved, it was useful to explain the origins of highly ordered CNC structures assembled on flat surfaces. Most importantly, the proposed methods enabled the production of continuous films, which is in clear contrast to previous efforts. Finally, it is hoped that the results will help on-chip manipulation and further assembly of CNCs with n-DEP forces.^[54]

2.5. Spontaneous polarization of cellulose nanocrystals using quantum-mechanical approach

Beside the well-known Clausius-Mossotti polarization calculation powerful and accurate *ab initio* quantum-mechanical methods have been developed for the calculation of piezoelectric response of different materials. The latter method includes also the polarization calculation, but with a different approach. The Clausius-Mossotti polarization calculation predict physical properties of biological cells and inorganic particles as well with a homogeneous discrete properties of a colloid like particle. The quantum-mechanical method uses individual, elemental crystal properties, which exploit the theory of Berry phases developed by Vanderbilt^[55,56], Resta^[57] and co-workers.

Two dependent non-zero piezoelectric constants ($e_{14} = e_{25}$) in the monoclinic and triclinic phase characterize the full piezoelectric tensor of such cellulose nanocrystals. The calculation of shear components of the phases have never been included in previous work. It therefore important to fill this gap and to compute the full piezoelectric tensor e_{ik} of cellulose nanocrystals. The second aim of this paragraph was to compare the piezoelectric behavior of the cellulose nanocrystals with the experimental results obtained from cellulose nanocrystal thin film piezo evaluation.

The quantum-mechanical method is based on the periodic linear combination of atomic orbitals (LCAO) approach, where crystalline orbitals are expanded over the basis sets of localized functions (atomic orbitals)^[58], which means that molecular orbitals are formed as a linear combination of atomic orbitals:

$$\psi_i = \sum_{\mu=1}^n c_{\mu i} \phi_{\mu} \quad (2.15)$$

where ψ_i is the i -th molecular orbital, $c_{\mu i}$ are the coefficients of linear combination, ϕ_{μ} is the μ -th atomic orbital, and n is the number of atomic orbitals, which are solutions of Hartree-Fock equations (a wave functions for a single electron in the atom).

In the calculation all of the atomic orbital sets was employed with different Gaussian contractions and eigenvalues and eigenfunctions were calculated by the Hartree-Fock (HF) and Density-Functional-Theory (DFT)

Hamiltonians functions. The Berry phase's theory (BP) of polarization were calculated according to the following equation (2.16):

$$\varphi_h^{(\varepsilon)} = (2\pi V/|e|)\mathbf{P} \cdot \mathbf{a}_h^* = (V/4\pi^2) \sum_n \int \langle u_n(\mathbf{K}) | -i\mathbf{a}_h^* \nabla_{\mathbf{K}} | u_n(\mathbf{K}) \rangle d\mathbf{K} \quad (2.16)$$

where V is the direct unit-cell volume (333.378 \AA^3 for triclinic unit cell of cellulose), $|e|$ is the electron charge, \mathbf{a}_h^* is the h -th reciprocal lattice basis vector, n is the electron band index, \mathbf{K} is the wave vector in the first Brillouin zone, and $u_n(\mathbf{x}, \mathbf{K}) = \psi_n(\mathbf{x}, \mathbf{K}) \exp(i\mathbf{K} \cdot \mathbf{x})$, where $\psi_n(\mathbf{x}, \mathbf{K})$ is the n -th crystalline orbital (eigenfunction of the one-electron Hamiltonian).

The lattice constants (in \AA) of triclinic unit cell of cellulose (Fig. 2.9.) used in the calculations are as follows: $a = 10.4001$, $b = 6.7176$, $c = 5.9627$, $\alpha = 80.375^\circ$, $\beta = 118.085^\circ$, $\gamma = 114.805^\circ$ ^[2]. The polarization is calculated in the transverse direction at zero electric field by a uniform shear strain. The sign of piezoelectric tensor is fixed assuming that the positive direction of y and z axis goes from the cation to the anion.

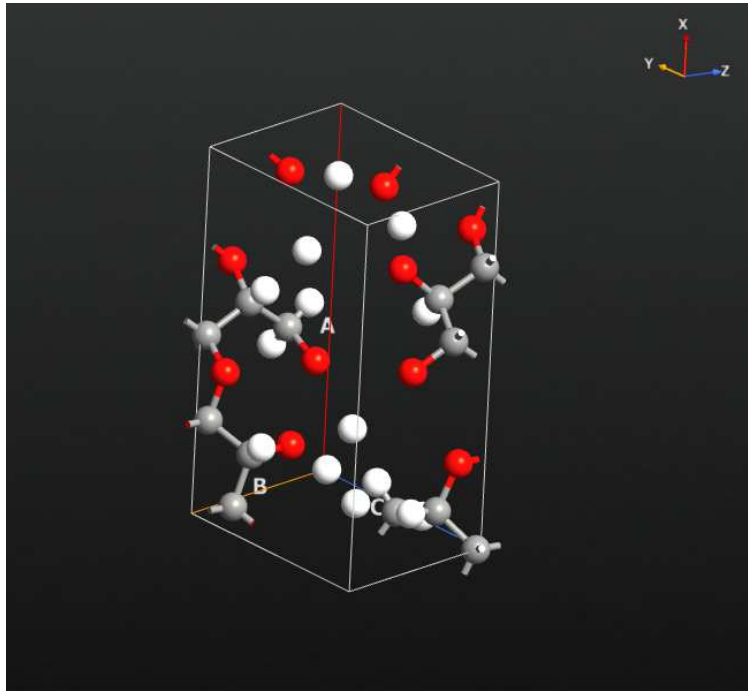


Figure 2.9. The figure shows a triclinic cellulose unit cell arrangement according to Nishiyama et al. 1997.

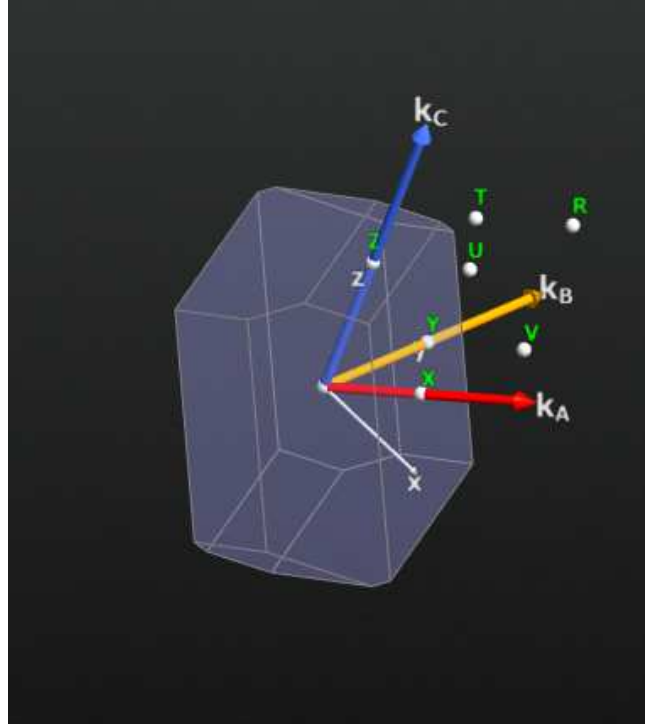


Figure 2.10. Some important symmetry points on the Brillouin zone of the triclinic cellulose crystal (real space) and direction of planes

All of the following parameters \mathbf{P} , \mathbf{a}_h^* , V and $u_n(\mathbf{K})$ are depend on the $\varepsilon = [\varepsilon_1, \varepsilon_2, \varepsilon_3, \varepsilon_4, \varepsilon_5, \varepsilon_6]$ strain tensor state (in Voight's notation). The two dependent piezoelectric constants e_{ik} ($e_{14} = e_{25}$) can be calculated using the equations above. It ensues, in the most general case, that

$$\partial P_i / \partial \varepsilon = \sum_k \alpha_k \partial P_i / \partial \varepsilon_k = \sum_k \alpha_k e_{ik} \quad (2.17)$$

By symmetry reasons:

$$e_{ik} = (1/\alpha_k) \partial P_i / \partial \varepsilon. \quad (2.18)$$

In order to avoid a multivalued problem, the polarization is not computed directly, it is evaluated from the BP's on the basis of reciprocal lattice vector. The reciprocal lattice is a collection of point that represents allowed values of wavevectors for Fourier series and Fourier transformations with the

periodicity of the lattice. Then the correct piezoelectric constant can be calculated from:

$$e_{ik} = (|e|/2\pi V\alpha_k) \sum_j \alpha_{ji} \partial \varphi_j / \partial \varepsilon. \quad (2.19)$$

For the calculation of polarization and piezoelectric tensor QuantumWise software with VNL-ATK script interphase has been used.

The polarization of material is divided into electronic and ionic part:

$$P_t = P_i + P_e. \quad (2.20)$$

The latter is calculated using a simple classical electrostatic sum of point charges:

$$P_i = \frac{|e|}{\Omega} \sum_v Z_{ion}^v r^v \quad (2.21)$$

where Z_{ion}^v and r^v are the valence charge and position vector of atom v , Ω is the unit cell volume and the sum runs over all ions in the unit cell. The ionic polarization part (P_i) of the modelled cellulose triclinic unit cell is 0.46, -0.069 and -0.31 in the x,y and z direction respectively, where the longest cell unit is coincide with the a lattice parameter (see Fig. 2.9.).

The electronic contribution to the polarization is obtained as:

$$P_e = -\frac{2|e|\hbar}{(2\pi)^3} \int dk_{\perp} \sum_{n=1}^M \int_0^G \langle u_{k,n} | \frac{\partial}{\partial k_{\parallel}} | u_{k,n} \rangle dk_{\parallel} \quad (2.22)$$

The electronic polarization part (P_e) of the modelled cellulose triclinic unit cell is 0.32, -0.077 and 0.44 in the x,y and z direction respectively, where the longest cell unit is coincide with the a lattice parameter (see Fig. 2.9.).

The total polarization (P_T) of the modelled cellulose triclinic unit cell is -0.148, -0.042 and 0.0317 C/m^2 in the x, y and z Cartesian direction, respectively.

The calculated piezoelectric tensor assuming homogeneous strains. It is referred as clamped-ion piezoelectric tensor. The calculated shear piezoelectric stain values are 0.887 and 0.565 C/m^2 . These xy and xz strain values leads to a polarization in the z and y-direction respectively.

2.6. Conclusion

A convective assembly setup was used to produce highly oriented ultrathin films of CNCs under low electric fields. CNC orientation was observed to depend on the field strength and frequency and was calculated by assuming the dipole moment value for prolate ellipsoids and the Clausius Mossotti factor. The low electric field strength used in this investigation was observed to be suitable for the formation of unprecedented anisotropic, homogeneously oriented ultrathin films of CNCs.

The full polarization and piezoelectric tensor were computed for cellulose triclinic unit cell using Berry Phase, HF and DFT with VNL as the computational engine. We have shown that using modern *ab initio* techniques it is now possible to predict the value of the piezoelectric tensor in a computationally complex material such as cellulose. Finally, we have introduced the calculated polarization.

The results of the analytical and experimental works indicated the following conclusions:

1. It has been confirmed that convective shear assembly with low electric field can produce highly oriented (degree of orientation is 88%) ultrathin films of CNCs on mica substrate obtained from chemically digested ramie fibers.
2. It has been confirmed that the orientation of CNCs were depend on AC electric field strength and frequency assuming the dipole moment value for prolate ellipsoids and the Clausius Mossotti factor.
3. It has been confirmed that the low AC electric field strength (800 V/cm, 2 kHz) and negative dielectrophoretic forces are suitable for unprecedented anisotropic, homogeneously oriented, extended ultrathin films of CNCs obtained from chemically digested ramie fibers.
4. It has been confirmed that quantum mechanical polarization approach techniques is now possible to predict the value of the piezoelectric tensor in a computationally complex crystalline material such as cellulose.

2.7. References

1. Y. Habibi, I.C. Hoeger, S. Kelley, O.J. Rojas, *Langmuir* 26 (2010) 990.
2. Y. Nishiyama, S. Kuga, M. Wada, T. Okano, *Macromolecules* 30 (1997) 6395.
3. E.D. Cranston, D.G. Gray, *Sci. and Tech. of Adv. Mat.* 7 (2006) 319.
4. D. Bordel, J.L. Putaux, L. Heux, *Langmuir* 22 (2006) 4899.
5. Y. Habibi, T. Heim, R. Douillard, *J. of Polym. Sci. B* 46 (2008) 1430.
6. N. Denkov, O. Velev, P. Kralchevski, I. Ivanov, H. Yoshimura, K. Nagayama, *Langmuir* 8 (1992) 3183.
7. B.G. Prevo, D.M. Kuncicky, O.D. Velev, *Colloids Surface A* 311 (2007) 2.
8. R. H. Atalla, D.L. VanderHart, *Science* 223 (1984) 283.
9. D.L. Van der Hart, R.H. Atalla, *Macromolecules* 17 (1984) 1465.
10. J. Sugiyama, T. Okano, H. Yamamoto, F. Horii, *Macromolecules* 23 (1990) 3196.
11. Y. Habibi, L.A. Lucian, O.J. Rojas, *Chem Rev.* (2010) DOI 10.1021/cr900339w
12. I. Hoeger, O. Velev, Y. Habibi, S. Kelley, O.J. Rojas, 239th ACS National Meeting, San Francisco, CA, 2010. March 21-25.
13. I.C. Hoeger, O.J. Rojas, K. Efimenko, O.D. Velev, S. Kelley, *Soft Matter* 7 (2011) 1957.
14. H. Asai, N. Watanabe, *Biopolymers* 15 (1976) 383.
15. C.D. Edgar, D.G. Gray, *Cellulose* 10 (2003) 299.
16. M.E. Leunissen, H.R. Vutukuri, A. van Blaaderen, *Adv. Mater.* 21 (2009) 3116.
17. J. Sugiyama, H. Chanzy, G. Maret, *Macromolecules* 25 (1992) 4232.
18. L.E. Helseth, *Langmuir* 21 (2005) 7276.
19. J.F. Revol, L. Godbout, X.M. Dong, D.G. Gray, H. Chanzy, G. Maret, *Liq. Cryst.* 16 (1994) 127.
20. F. Kimura, T. Kimura, M. Tamura, A. Hirai, M. Ikuno, F. Horii, *Langmuir* 21 (2005) 2034.
21. T. Ebeling, M. Paillet, R. Borsali, O. Diat, A. Dufresne, J.Y. Cavaille, H. Chanzy, *Langmuir* 15 (1999) 6123.
22. J.O. Zoppe, M.S. Peresin, Y. Habibi, R.A. Venditti, O.J. Rojas, *ACS App. Mater. Interfaces* 1 (2009) 1996.

23. J. Gimsa, D. Wachner, *Biophys. J.* 77 (1999) 1996.
24. S.S. Dukhin, *J. Surf. Coll. Sci.* 3 (1970) 83.
25. T.B. Jones, G.A. Kallio, *J. Electrostatics* 6 (1979) 69.
26. B. Khusid, A. Acrivos, *Phys. Rev. E* 52 (1995) 1669.
27. D. Mietchen, T. Schnelle, T. Müller, R. Hagedorn, G. Fuhr, *Journal of Physics D: Applied Physics* 35 (2002) 1258.
28. M. Castellarnau, A. Errachid, C. Madrid, A. Juárez, J. Samitier, *Biophys. J.* 91 (2006) 3937.
29. K.R. Foster, H.P. Schwan, in *Handbook of Biological Effects of Electromagnetic Fields*, (Eds. C. Polk and E. Postow), CRC Press Inc., Boca Raton, Fl. 25-102.
30. H.A. Pohl, *J. Appl. Phys.* 22 (1951) 869.
31. J. Gimsa, P. Marszalek, U. Löwe, T.Y. Tsong, *Biophys. J.* 60 (1991) 749.
32. U. Zimmermann, W.M. Arnold, *Coherent Excitations in Biological Systems*, (Eds. H. Fröhlich, F. Kremer), Springer-Verlag, Berlin 1983, pp. 211-221.
33. T. Kakutani, S. Shibatani, M. Sugai, *Bioelectrochem. Bioenerg.* 31 (1993) 131.
34. V. Ph. Pastushenko, P.I. Kuzmin, Yu. A. Chizmadzhev, *Biol. Membr.* 5 (1988) 65.
35. L.D. Landau, E.M. Lifshits, *Electrodynamics of Continuous Media*, Moscow, Nauka [in Russian] 1982, 624 p.
36. Application Note 1217-1, "Basics of measuring dielectric properties of materials" Hewlett-Packard [1992]
37. S. Boutros, A. A. Hanna, *J. of Polym. Sci.* 16 (1978) 89.
38. M. Nilsson, G. Frenning, J. Grasjo, G. Alderborn, M. Stromme *J. Phys. Chem. B* 110 (2006) 20502.
39. W.N. Stoops, *J. Am. Chem. Soc.*, 56 (1934) 1480.
40. A.H. Salama, M. Dawy, A.M.A. Nada, *Polymer-Plast. Technol.* 43 (2004) 1067.
41. A.V. Sokirko, *Biol. Mem.* 6 (1992) 587.
42. P.E. Trout, PhD Thesis, Lawrence College, cited in *Paper Chemistry*, J. C. Roberts, editor, Blackie Academic and Professional, London, 1951, pp. 249.

43. A.S. Dimitrov, K. Nagayama, *Langmuir* 12 (1996) 1303.
44. E. Adachi, A.S. Dimitrov, K. Nagayama, *Langmuir* 11 (1995) 1057.
45. T.B. Jones, *Electromechanics of particles*, Cambridge University Press, New York, NY 1995
46. J.C. Slater, *Introduction to chemical physics*, McGrawHill Press, 1939
47. M. Parthasarathy, D.J. Klingenberg, *Mater. Sci Eng.* 1996, 17
48. L.C. Davis, *J. Appl. Phys.* 72 (1992) 1334.
49. L.C. Davis, *Appl. Phys. Lett.* 60 (1992) 319.
50. R.A. Anderson, in (Ed. R. Tao *Electrorheological Fluids, Mechanisms, Properties, Structure, Technology, and Applications*), Proc. of the Int. Conf on Electrorheological fluids, Carbondale, Illinois, USA, 15-16 October, 1991, World Scientific, Singapore, 1992
51. M. Mittal, E.M. Furst, *Adv. Funct. Mater.* 19 (2009) 3271.
52. V. Canpean, S. Astilean, T. Petrisor, M. Gabor, I. Ciascai, *Mater. Lett.* 63 (2009) 1834.
53. B.G. Prevo, O.D. Velev, *Langmuir*, 20 (2004) 2099.
54. O.D. Velev, K.H. Bhatt, *Soft matter*, 2 (2006) 738.
55. R.D. King-Smith, D. Vanderbilt, *Phys. Rev. B* 47 (1993) 1651.
56. D. Vanderbilt, *J. Phys. Chem. Solids* 61 (2000) 147.
57. R. Resta, *Rev. Mod. Phys.* 66 (1994) 899.
58. M. Catti, Y. N. R. Dovesi, *J Phys Chem Solids* 64 (2003) 2183-2190.

Chapter 3

Ultrathin piezoelectric films of cellulose nanocrystals prepared by electric field-assisted shear assembly**3.1. Introduction**

Asymmetric crystalline structures can display inhomogeneous deformation of strain gradients, associated with the piezoelectric response due to an applied electric field. Biopolymer structures with such property include cellulose, which can be used as soft electroactive material. Thus, cellulose nanocrystals (CNCs), nanoparticles of low density, high mechanical strength, thermal stability, chemical resistance, and biocompatibility^[1] can be potentially used in components requiring a piezoelectric response, including sensors and actuators, biomedical devices, and so forth.

Piezoelectricity is related to the change in polarization (electrical charge) density and the occurrence of dipole moments within a material. It has been generally considered of significance only in highly crystalline materials. The piezoelectric effect in wood was first reported by Bazhenov in 1950.^[2] However, the magnitude of the piezoelectric constant in fibers and wood is small mainly due to the random, heterogeneous distribution and a relatively small amount of crystalline cellulose in the lignocellulose matrix. The experimental verification of both direct and inverse piezoelectric effects and quantification of the constants in the piezoelectric matrix were carried out by Fukada in 1955.^[3] Only the shear piezoelectric constants $-d_{14} = d_{25}$ are finite while the other components are zero, according to uniaxially oriented system of cellulose crystallites. Different wood species show considerably different piezoelectric properties. Further, the piezoelectricity of a given species varies depending on factors such as density, percentage of latewood, and so forth.^[4] The piezoelectric modulus upon heat treatment of spruce increases initially and then decreases, following changes in crystallinity.^[5] Hydration also plays a role since it has been shown that the piezoelectric

constant of bamboo in the dry state is larger than that in hydrated form.^[6] The piezoelectricity in chemical wood pulps, cotton, and cellulose derivatives such as cellophane, celluloid, and viscose rayon has been reported to depend on the fibril orientation.^[7] The piezoelectric constant of regenerated nanocrystalline cellulose (II) was measured to be 35–60 pC/N, which was considered suitable for energy harvesting and power generation.^[1]

Ultrathin films of CNCs have been manufactured by several methods.^[8–21] **Therefore, given the native crystalline nature of CNCs it is reasonable to ask the question if they can collectively yield a large piezoelectric effect. Could this specially be the case in films of highly aligned CNCs? Could such films induce high energy conversion and piezoelectricity? Could such films be modelled using finite element modelling environment?** If this was the case, films or materials made with aligned CNCs could be useful to produce and detect sound, to generate voltage, or to manufacture nanosensors, actuators, microbalances, devices for ultrafine optical focusing, and so forth.^[22] The deconstruction of fibrillar cellulose by acid hydrolysis yields cellulose nanocrystal rod-like, highly crystalline nanoparticles.

In studies related to the piezoelectric behavior of cellulose fibers, different preparation and modification routes as well as characterization techniques have been considered.^[23,24] Corona poled electro-active paper made from cellulose, cyanoethylated cellulose, and LiCl-DMAc modified cotton (0.32 index of crystallinity) were reported to have piezoelectric constants of 0.167,^[23] 0.1–0.2,^[25] and 0.16^[25] Å/V, respectively. Such previous work involved the use of cellulose (in fibers or in composites) combined with chemical additives or electrolytes to allow the piezoelectric response; however, to our knowledge ultrathin films of CNCs has not been considered yet. Therefore, our present work explores the effective piezoelectric coefficient d_{25} of CNCs assembled in ultrathin films which were previously manufactured by a combination of shear and electric fields. The degree of alignment of the CNCs within the films (as a function of voltage, frequency, and shear used during their manufacturing) is proposed to allow control of the piezoelectric behavior of the system and produce a large piezoelectric response.

The dielectrophoretic properties of CNCs were investigated and reported in a recent contribution.^[26] The dipole density or polarization of CNCs was

calculated by summing up the dipole moments per volume of the crystallographic unit cell.^[27] The Clausius—Mossotti factor allowed the description of the critical and characteristic frequencies as well as the peak dielectrophoresis of CNCs. We also determined the optimal field strength for isotropic alignment in thin films. Using the same methods of our previous work,^[21] we obtained ultrathin films of aligned CNCs. By using shear forces coupled with externally applied electric fields we investigated the effect of alignment on the piezoelectric response of the CNC film.

The polarizability of CNCs under uniform electric fields and shear forces during withdrawal of a deposition plate induced alignment. Mica was used as solid support for the CNCs.^[21] Two reference films were obtained, without application of electric field, and used to elucidate the influence of the solid support. Film formation was observed to depend on the withdrawal rate as well as rate of solvent (water) evaporation. Homogeneous CNC deposition was observed when the solid support was modified with a positively charged polymer layer. Thus, preadsorption of low molecular weight polyethyleneimine (PEI) was used to facilitate a linear growth of ultrathin films of CNCs on mica. The buildup of single or multiple layers of CNCs depended on the concentration of the dispersion and other factors. The length of the deposited CNC films on mica with preadsorbed PEI was 5 cm. The typical film thickness and root-mean-square roughness (atomic force microscope, AFM) were of the order of 38 and 2.5–3 nm, respectively.

Given the highlighted objectives, the first part of this chapter resulted three peer reviewed scientific publications in *ACS Macro Letters* (a Q1 qualified journal) Vol. 1 in 2012, pages: 867-870 and *Journal of Colloid and Interface Science* (a Q1 qualified journal), Vol. 363 in 2011, pages: 206-212 and in *Cellulose* Vol. 22 pages 779-788 in 2015. The second part of that chapter has been worked out as an extension of the previous work using the finite element modeling approach for the utilization of piezoelectric coefficient in engineering applications.

3.2. Materials and methods

3.2.1. Cellulose Nanocrystals

Ramie fibers from Stucken Melchers GmbH & Co., Germany, were used in the production of CNCs. The detailed procedure can be found in our previous communication;^[34] briefly, ramie fibers were purified with a Soxhlet extraction system and then hydrolyzed with 65 % sulfuric acid at 55 °C for 30 min under continuous stirring. Deionized water from an ion-exchange system (Pureflow, Inc.) followed by treatment in a Milli-Q® Gradient unit with a resultant resistivity of $>18 \text{ M}\Omega\cdot\text{cm}$ was used. The CNC suspension was filtered through a sintered Buchner funnel, washed with water and recovered by subsequent centrifugations at 10,000 rpm (10 °C) for 10 min each. The CNC suspension was dialyzed against deionized water and then against Milli-Q water for a few weeks. The obtained CNC suspension was stored at 4 °C until use. The dimensions of the CNCs were $185 \pm 25 \text{ nm}$ in length and $6.5 \pm 0.7 \text{ nm}$ in width, as determined by transmission electron microscopy.²⁶ The particles were confirmed to be 88% crystalline as determined by WAXS.

3.2.2. Manufacture of CNC films

Aqueous CNC suspensions of 2.5 wt% concentration were used to make the thin films by using a shear/convective assembly setup combined with an externally-applied AC electric field. A withdrawal speed of 8.4 cm/h was used for obtaining highly oriented films.^[12,21] The AC electric field was generated by a power amplifier (Krohn-Hite M7500 wideband power amplifier) driven by a sine wave from a function generator (Wavetek M134). The reported voltages are peak-to-peak values. Microscope glass slides were used as support for thin sheets of freshly cleaved mica, which were used to deposit the CNCs. To this end mica sheets were gently glued onto the glass slides and the topmost layer was peeled off to uncover a clean, pristine mica surface. Before CNC assembly, the glass-mica solid support was treated with a 500 ppm polyethyleneimine (PEI) solution, which made cationic charges available for electrostatic interactions with the negatively charged CNCs. In the course CNC assembly, a droplet (ca. 20 μl) of liquid suspension was

placed in the wedge formed by a tilted (24°) glass slide (deposition plate) and the mica support (Figure 3.1). The CNC suspension was held by capillary forces and the liquid meniscus was withdrawn horizontally across the mica support by translating the tilted glass slide. This translation was produced with a syringe pump (NE-500 New era pump systems, Inc, Wantagh, NY) that moved the tilted glass at a constant speed of 8.4 cm/h. To create the constant AC electric field around the mica carrier, two parallel aluminum electrodes spaced 5 mm apart from each other were placed on the edges of the mica sheet and connected to a power amplifier. The CNC film deposition was carried out at 50 % relative humidity and 23°C . The system was driven by a computer, allowing precise control of the withdrawal speed. AC electric fields with strengths of 100, 400 and 800 V/cm and frequencies of 45, 200 and 2000 Hz were used.

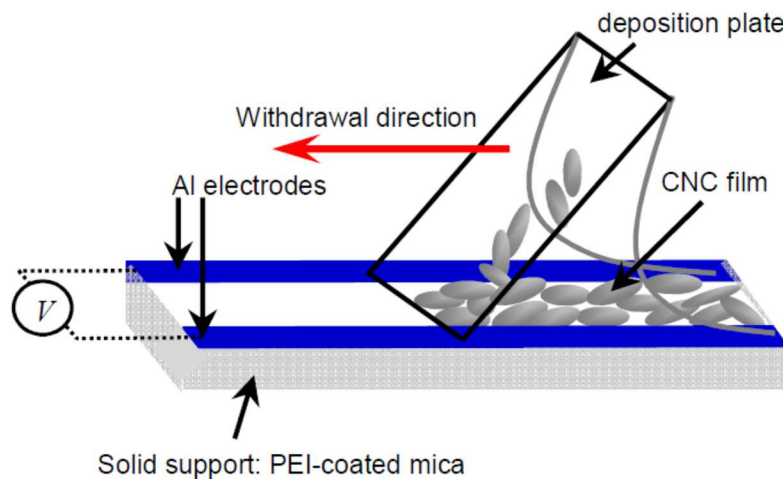


Figure 3.1. Schematic illustration of the shear/convective assembly setup used to manufacture CNC films under a coupled electric field. In a typical experiment, a volume of CNC suspension is placed between a tilted, deposition glass slide and a base substrate consisting of mica with preadsorbed PEI and supported on a glass slide. The distance between the aluminum electrodes was 5 mm. The withdrawal velocity of the deposition glass slide in the horizontal direction was kept constant at 8.4 cm/h.

Typical CNC film thicknesses were estimated to be of the order of 38 nm (surface roughness mean 4 nm) and therefore they consisted of CNC multilayer structures (approximately 6 layers, considering the measured CNC dimensions). The degree of CNC alignment was obtained by analyzing AFM images. A Matlab code was used for image processing and analyses that facilitated CNC identification, particle count and CNC orientation angle of the longest axis of the nanoparticles with respect to the withdrawal direction (Figure 3.1).

3.3. Piezoelectric measurement

A high degree of CNC orientation in the films is a key characteristic for the piezoelectric response. AC electric fields (10 Hz) of different strengths were applied on the dried films, which resulted in strain due to the converse piezoelectric effect. Piezoelectric measurements were performed in contact mode by measuring the deflection of the AFM tip in a Quesant Q-Scope AFM (x – y scans were disabled; see Figure 3.2). Commercially available conducting diamond AFM tips were used to avoid electrostatic interaction between the tip and the sample. These experiments were carried out in an environment with constant relative humidity (50%) and temperature (23 °C). The bottom electrode, underneath the CNCs films fixed on the AFM stage, was connected to a signal generator using commercially available BNC cables. For the top electrode, a copper probe was used. Each measurement lasted ca. 30 s. The AFM tip deflection in the z -direction (extension or contraction) was recorded using a built in lock-in amplifier. To avoid the tip–sample electrostatic interaction, the AFM stage was grounded. For the piezoelectric measurement a 10 Hz sin frequency signal was employed using Wavetek M134 signal generator; this frequency was selected on the basis that it is below the tip resonance and most environmental noise (20–200 Hz). The peak-to-peak voltage was varied by 2.5 V units with a maximum value of 20 V. During the experiment at one given voltage, 7–10 displacement measurements were carried out, and the averaged value was used in the calculation. The piezoelectric constant was calculated from the correlation slope of the measured tip displacement at the applied voltage. Reference measurements were performed on (420 nm) ZnO thin films. The ZnO film was obtained from deposition on silica wafer using an argon

sputtering technique, and platinum (Pt, 164 nm) is used as the bottom electrode.

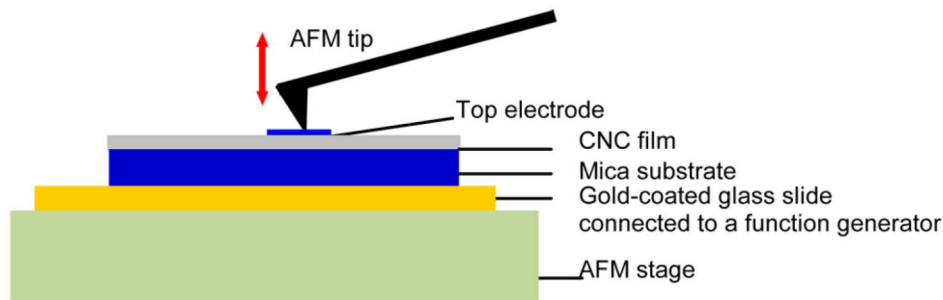


Figure 3.2. Schematic illustration of the AFM system used to measure the displacement of CNC films in contact with an AFM diamond tip and under given applied voltages (10 Hz frequency).

3.4. Results and discussion

The piezoelectric response from the CNC film was monitored by measuring the height deflection by using a conductive AFM diamond tip. The 10 Hz signals of low and high voltage resulted in deflection perpendicular to the z direction of the film, as observed in Figure 3.3. Three different sections are shown in this figure to represent the cyclic (on— off) response of the film subject to three different alternating voltages (10 Hz): 10 V (upper section), 15 V (middle section), and 0 V (bottom section). According to the shift in height as a result of changes in AC electric fields, the strain response of the film was found to be linear and non hysteretic. To our knowledge, no detailed work related to piezoelectricity of crystalline cellulose or CNC films is available to date. Thus, this contribution provides the first experimental results showing that CNCs display such piezoelectric effects.

Piezoelectric experiments were performed on four different supported CNC films, with different degrees of particle alignment. For a given voltage 7—10 repetitions were performed and the average used to calculate the piezoelectric constant (Figure 3.4). A linear correlation between the measured effective displacement and the applied voltage was observed.

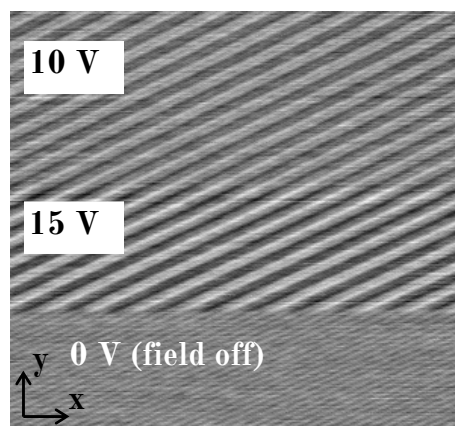


Figure 3.3. Map showing the extent of CNC film wavy displacement (z direction, perpendicular to the surface) as a result of their piezoelectric effect. The extent of displacement is indicated by lighter or darker fields as monitored by an AFM (conductive) diamond tip in contact with the film. A single point was monitored under given intermittent electric fields (10, 15, and 0 V). The deflection measured was used to calculate the piezoelectric constant of the films. The x and y scales in the image are dimensionless but indicate film deflection evolution with time as the voltage is turned on and off (see Figure 3.2 for the experimental setup).

The values reported in Figure 3.4 were corrected for the contribution from the solid support (mica sheet on gold-coated glass wafer). Films of partly aligned CNCs (obtained by electric field assisted-shear at 800 V/cm, 45 Hz) yielded a piezoelectric constant of $0.97 \text{ \AA}/\text{V}$. A similar value, $1.10 \text{ \AA}/\text{V}$, was obtained with films manufactured under slightly lower electric field strength and higher frequency (400 V/cm and 200 Hz).

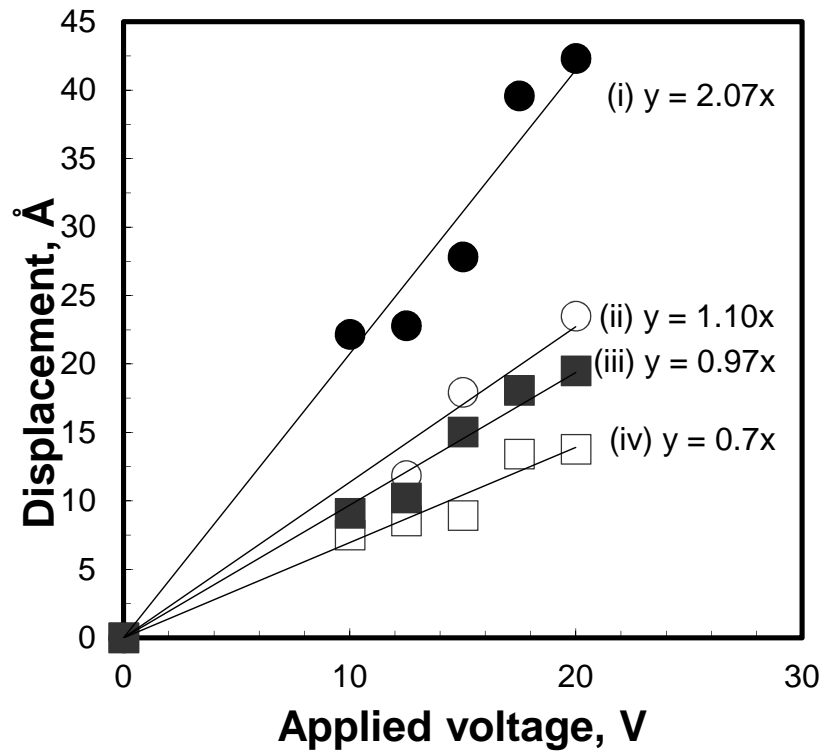


Figure 3.4. Vertical displacement of CNC films subject to externally applied electric fields. Included are results for films produced under four different conditions during electric field-assisted shear (films i–iv, Table 3.1). The films with the higher degree of alignment produced a higher piezoelectric response, as indicated by the slopes of the profiles. The displacements and voltages are both peak-to-peak values.

The respective degree of alignment for these films was 42 and 46%, respectively (Table 3.1). CNC films with a higher degree of alignment (88% alignment degree obtained under assembly at 800 V/cm and 2 kHz) yielded a higher piezoelectric response, 2.10 Å/V.

Table 3.1. Field Strength and Frequency Used during the Manufacture of CNC Films (i–iv) by Using an Electric Field-Assisted Shear Assembly Setup^a

Sample	Field strength [V/cm] / frequency [Hz]	degree of alignment of CNCs [%] ²⁶	piezoelectric coefficient (d_{25})
i	800 / 2000	88	2.10
ii	400 / 200	46	1.10
iii	800 / 45	42	0.97
iv	100 / 2000	77	0.7

^aThe degrees of alignment of the obtained films as well as measured piezoelectric coefficient d_{25} are reported (see Figure 3.2).

Thus, the alignment of polarization gradient in CNC films increased the electromechanical actuation and strain. When CNCs were aligned perpendicular to the withdrawn direction (100 V/cm at 2 kHz), a lower piezoelectric coefficient of 0.7 Å/V was measured (Table 1). Despite the expected high particle rotation at the high frequency (2 kHz), the low field strength in this case (100 V/cm) was not sufficient to effectively polarize the nanoparticles.

An explanation for the observed high piezoelectric constant of CNC films comes from the native crystalline cellulose, which comprises chains arranged parallel with a 2-fold screw symmetry along the chains due to the β -1,4 linkage of the D-glucose subunits.^[28,29] The piezoelectricity of cellulose is due to the anisotropic triclinic and monoclinic unit^[30–32] crystal structure association with unevenly distributed carbon atoms and change of polarization density of charged atomic groups under electric fields. This involves the occurrence of electric dipole moments within the CNC particles. The triclinic unit cell of Sugiyama et al.,^[31] first suggested by Sarko and Muggli as a two-chain cell,^[32] has a single-chain P1 structure, with adjacent molecules shifted monotonically by one-quarter of the unit cell size in the c direction. In the two-chain monoclinic unit cell, the corner chain is shifted $c/4$ (c axis is perpendicular to the a and b crystalline plane here) relative to the center chain, such that the overall configuration displays staggering of adjacent chains.

A key observation is the fact that the piezoelectric response of CNC films changes as a function of CNC alignment. However, the identification of the detailed mechanism for the piezoelectric effect is beyond the scope of this

study. However, it is associated with the dipolar orientation, the crystallinity and alignment of CNCs in the films. More specifically, the piezoelectricity of CNC particles involves the occurrence of electric dipole moments within the particles; this may be associated with unevenly distributed carbon atoms and change of polarization density of charged atomic groups under electric fields within the anisotropic crystalline structure of cellulose I. Overall, the naturally long-range ordered polymer chains and its polarizability are responsible for the observed high shear piezoelectricity.

The calculation of the ratio of the overall macromolecular charge and crystal skeleton constant indicates that CNCs have high flexoelectrical capacity. We note that the CNCs lie flat on the solid support and the bottom gold-coated glass slide serve as electrode. When the signal generator applies different voltages between the top and bottom electrodes, a strain of 0.02–0.1% is induced in the film, leading to a vertical displacement of the film. Such displacement $D_{i,j,k}$, due to the external electric field can be determined by eq 3.1:

$$D_{i,j,k} = d_{i,j,k} \sigma_{i,j,k} \quad (3.1)$$

where d is the piezoelectric coefficient and σ is the tensile stress. The displacement is related to the generated charge by the following relation

$$q = \iint D_{i,j,k} dA_{i,j,k} \quad (3.2)$$

where dA is an infinitesimal electrode area normal to the displacement. If we consider that the piezoelectric effect is reversible, the applied voltage (or generated voltage from the strain), V , can be related by the capacitance of the thin CNC film ($C_{\text{CNC film}}$):

$$V = q/C_{\text{CNC film}} \quad (3.3)$$

with

$$C_{CNC\ film} = \frac{\epsilon_{cell} \epsilon_0 l_{CNC\ film} w_{CNC\ film}}{t_{CNC\ film}} \quad (3.4)$$

Here ϵ_{cell} is the relative permittivity of cellulose (4.032 F/m), ϵ_0 is the vacuum permittivity (8.85×10^{-12} F/m), and the dimensions of the thin film are $l_{CNC\ film} = 5 \times 10^{-2}$, $w_{CNC\ film} = 5 \times 10^{-3}$, and $t_{CNC\ film} = 38 \times 10^{-9}$ m corresponding to the length, width, and thickness, respectively. The calculated capacitance is thus ~ 235 nF. Using the measured displacement of the film it is possible to calculate the known, applied voltage using eq 3.3 in one direction only:

$$V = \frac{d_{14} \sigma dA}{C_{CNC\ film}} = \frac{d_{14} E t_{CNC\ film}}{C_{CNC\ film}} \int \epsilon t_{CNC\ film} dt \quad (3.5)$$

where E is the elastic modulus of nanocrystalline cellulose (assumed to be 137 GPa¹¹). Equation 3.5 results in a calculated applied voltage on the thin film of 23.9 mV. Thus, the range of applied voltages (10–20 V) used for generating the piezoelectric displacement seems sufficient enough for 10% measurable strain in the film in the perpendicular direction of the c axis. As the film thickness increases, a lower capacitance and hence a higher generated output voltage or piezoelectric response can be expected. However, further investigation needs to be carried out to elucidate more details about the effect of the CNC thin film thickness. We note that the inherent structure (CNC alignment) of the thin film was not considered in this calculation, and therefore the results are only provided as a guesstimate.

Some of the CNC films tested here yielded a piezoelectric constant which was higher than the d_{33} value measured for a 400 nm ZnO film, 1.3 Å/V. This latter experimental value was in agreement with reported figures and provided verification of our measurement system.^[33] Note that the piezoelectricity of ZnO thin films is thickness- and crystal orientation-dependent; hence Ar sputtering of the ZnO thin film can enhance c -axis orientation and the piezoelectric constant.

Thinking further eq. (3.1), the so-called coupling equations can be combined considering the Hook's law of linear elastic materials, which results the strain-charge form of linear piezoelectricity:

$$S = sT + \partial^t E \Rightarrow S_{ij} = s_{ijkl}T_{kl} + d_{kij}E_k \quad (3.6)$$

$$D = \partial T + \varepsilon E \Rightarrow D_i = d_{ijk}T_{jk} + \varepsilon_{ij}E_j \quad (3.7)$$

where, S is strain, s is the compliance, T is stress tensor. The strain-charge for a material with *Hermann-Mauguin* notations: $P1(1, \bar{1}, 2, \bar{2} = m, 2/m)$ crystal classes (triclinic and monoclinic) like cellulose nanocrystals can be written:

$$\begin{bmatrix} S_1 \\ S_2 \\ S_3 \\ S_4 \\ S_5 \\ S_6 \end{bmatrix} = \begin{bmatrix} s_{11}^E & s_{12}^E & s_{13}^E & 0 & 0 & 0 \\ s_{21}^E & s_{22}^E & s_{23}^E & 0 & 0 & 0 \\ s_{31}^E & s_{32}^E & s_{33}^E & 0 & 0 & 0 \\ 0 & 0 & 0 & s_{44}^E & 0 & 0 \\ 0 & 0 & 0 & 0 & s_{55}^E & 0 \\ 0 & 0 & 0 & 0 & 0 & s_{66}^E \end{bmatrix} \begin{bmatrix} T_1 \\ T_2 \\ T_3 \\ T_4 \\ T_5 \\ T_6 \end{bmatrix} + \begin{bmatrix} 0 & 0 & 0 \\ 0 & 0 & 0 \\ 0 & 0 & 0 \\ d_{14} & 0 & 0 \\ 0 & d_{25} & 0 \\ 0 & 0 & 0 \end{bmatrix} \begin{bmatrix} E_1 \\ E_2 \\ E_3 \end{bmatrix} \quad (3.8)$$

Applying the cellulose characteristics and using the Young modulus (E) and Poisson's ratio (ν), the following strain-charge tensor can be obtained:

$$\begin{bmatrix} S_{11} \\ S_{22} \\ S_{33} \\ 2S_{23} \\ 2S_{13} \\ 2S_{12} \end{bmatrix} = \begin{bmatrix} \frac{1}{E_{11}} & \frac{-\nu_{21}}{E_{22}} & \frac{-\nu_{31}}{E_{33}} & 0 & 0 & \frac{\eta_{12,1}}{G_{12}} \\ \frac{-\nu_{12}}{E_{22}} & \frac{1}{E_{22}} & \frac{-\nu_{32}}{E_{33}} & 0 & 0 & \frac{\eta_{12,2}}{G_{12}} \\ \frac{-\nu_{13}}{E_{33}} & \frac{-\nu_{23}}{E_{33}} & \frac{1}{E_{33}} & \frac{1}{G_{23}} & \frac{\mu_{13,23}}{E_{22}} & \frac{\eta_{12,3}}{G_{12}} \\ 0 & 0 & 0 & 0 & \frac{1}{G_{13}} & 0 \\ 0 & 0 & 0 & 0 & 0 & \frac{1}{G_{12}} \end{bmatrix} \begin{bmatrix} T_{11} \\ T_{22} \\ T_{33} \\ T_{23} \\ T_{13} \\ T_{12} \end{bmatrix} + \begin{bmatrix} 0 & 0 & 0 \\ 0 & 0 & 0 \\ 0 & 0 & 0 \\ 0 & 0 & d_{14} \\ 0 & d_{25} & 0 \\ 0 & 0 & 0 \end{bmatrix} \begin{bmatrix} E_1 \\ E_2 \\ E_3 \end{bmatrix} \quad (3.9)$$

Dri et al.^[34] published the complex elastic compliance matrix for cellulose I_β (at 1, 1.5 and 2% strain, in [1/GPa] x 1000 unit) based on Nishiyama et al.^[35] initial structure with respect to the Cartesian system of coordinates. The following notation contain the experimentally obtained piezoelectric constant values as well in [$\text{\AA}/\text{V}$].

$$\begin{bmatrix} S_{11} \\ S_{22} \\ S_{33} \\ 2S_{23} \\ 2S_{13} \\ 2S_{12} \end{bmatrix} = \begin{bmatrix} 51.9 & -7.4 & -2.2 & 0 & 0 & 11.2 \\ -7.4 & 13.3 & -0.5 & 0 & 0 & -25.6 \\ -2.2 & -0.5 & 4.8 & 0 & 0 & 2.2 \\ 0 & 0 & 0 & 60.0 & -43.3 & 0 \\ 0 & 0 & 0 & -43.3 & 372.7 & 0 \\ 11.2 & -25.6 & 2.2 & 0 & 0 & 239.7 \end{bmatrix} \begin{bmatrix} T_{11} \\ T_{22} \\ T_{33} \\ T_{23} \\ T_{13} \\ T_{12} \end{bmatrix} + \begin{bmatrix} 0 & 0 & 0 \\ 0 & 0 & 0 \\ 0 & 0 & 0 \\ 0 & 0 & 2.1 \\ 0 & 2.1 & 0 \\ 0 & 0 & 0 \end{bmatrix} \begin{bmatrix} E_1 \\ E_2 \\ E_3 \end{bmatrix} \quad (3.10)$$

The elastic compliance matrix has been used for the FEM calculation in the next paragraph from eq. (3.10).

The direct piezoelectric parameters (Eq. 2.19) of cellulose nanocrystals can be converted using the following equation:

$$e_{ij} = \left(\frac{\partial D_i}{\partial S_j} \right)^E = - \left(\frac{\partial T_j}{\partial E_i} \right)^S \quad (3.11)$$

Eq. 3.11 resulted $e_{14} = -0.382$, $e_{25} = 0.609$ and $e_{15} = e_{24} = 0.441 \text{ C/m}^2$. The result implies that not only two identical shear piezo coefficient exist in cellulose nanocrystals, but three independent. The unit triclinic and monoclinic cell of cellulose is not symmetric, hence there should exist more than 2 shear piezoelectric coefficient.

3.5. CNC thin-film acoustic resonator modelling with FEM

In this section piezoelectric cantilever and composite acoustic resonator has been modeled using finite element eigenfrequency-response analysis. In both cases the piezoelectric layer was modeled as piezoelectric cellulose nanocrystal thin film using the previously measured piezoelectric constants.

The thin film resonators can be made from cellulose nanocrystal thin films, because they can be designed to have smaller acoustic wavelength in size than the electromagnetic wavelength compared with ceramic piezo crystals.

In the first arrangement – composite acoustic resonator –, cellulose nanocrystal active piezoelectric layer was formed on aluminum layer, which has been placed over on silica wafer. This aluminum layer served as bottom electrode and one more aluminum layer has been placed over the CNC layer for the upper electrode. Both aluminum layers are 0.2 μm thick and the piezoelectric layer is 9.5 μm thick. The width of the rectangular top electrode is 500 μm . The bottom carrier silicon wafer is roughly 1.7 mm wide. This arrangement has been modeled using a 2D model with Comsol Multiphysics software package. The build-up model contain different mechanical and electrical loss, damping factors in the piezoelectric layer. A structural loss factor represents the hysteresis in a stress-strain curve and a dielectric loss factor has been modeled with the polarization loss of the material. These structural and polarization loss values are imaginary components of the mechanical stiffness and relative permittivity. The parallel mode capacitance model was used and the DC conductivity (admittance) can be presented as $S=G+iB$ (G – conductance and B - susceptance).

The following Figure 3.5 shows lowest bulk acoustic mode of the resonator identified from the solutions of eigenfrequency analysis. The real part of the eigenfrequency is 82 kHz, which cause scaled deformation (2.39 μm) on the piezoelectric resonator and the imaginary part 16 kHz reflects to the damping due to the structural loss and polarization loss.

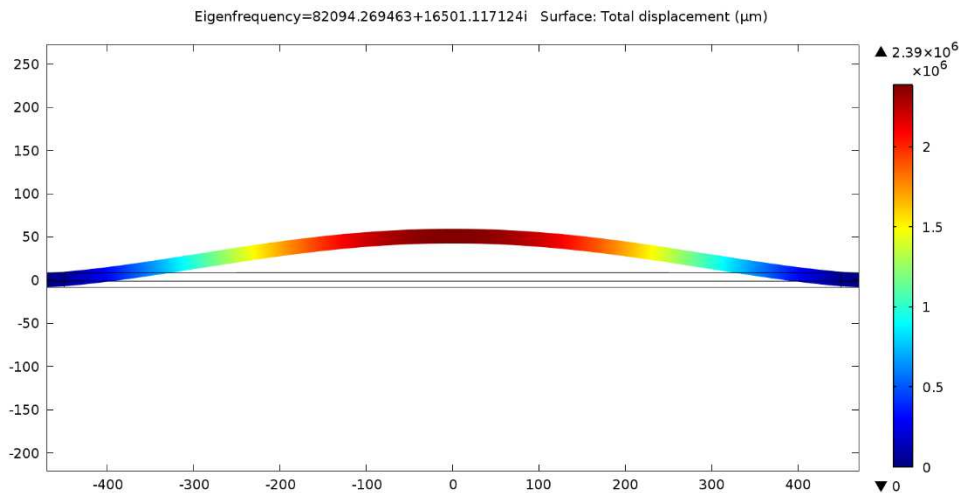


Figure 3.5. The lowest bulk acoustic mode, scaled deformation of the resonator identified from the solutions of the eigenfrequency analysis. The modeled geometry is a 1 mm section of the center of the resonator (horizontal and vertical axis dimensions are in μm).

The following Figure 3.5 shows the absolute value of admittance as a function of frequency. It can be seen that higher frequencies increase the global admittance in the whole modeled range of frequencies. Since the piezoelectric cellulose nanocrystal thin layer is an insulating part of the model, it can be concluding that this layer has a significant effect on conductivity. Similar effect has been observed on antocyanin and nano TiO_2 modified cellulose fiber sheet^[36]. Here the modelled admittance trend is very similar like that in the mentioned work. In the vicinity of the main resonance there is no any additional responses or side resonance, which could reduce the usability of the modeled resonator due to the only shear type piezo response of cellulose nanocrystals.

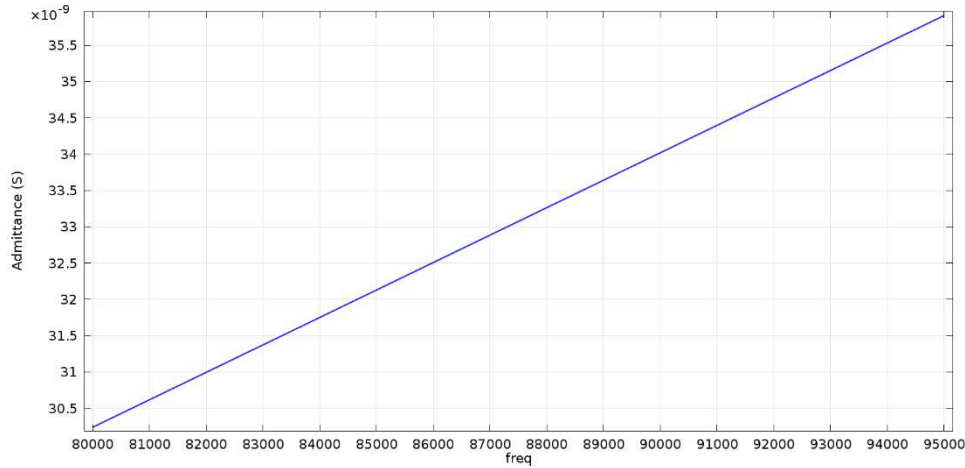


Figure 3.6. Absolute value of the admittance (dimensionless) vs. frequency (Hz).

The loss tangent ($\tan \delta = G/B$) values of the piezoelectric device tend to level at all frequencies and clearly exhibit a very low loss (data not shown). In this modeling set-up aluminum electrodes has been applied with perfect contact with CNC film, but in real experimental set-up it is not possible to perform and the cellulose nanocrystals tends to increase the potential barrier between the electrodes, extending from the Fermi levels of the metal to the bottom of the conduction band of the dielectric. The height of the barrier will depend on several factors such as Fermi levels and work functions of metal and insulator, the presence of shallow traps, the thickness of the insulator and its affinity towards the electrons^[37,38]. Since the metal has much lower work function than the insulator, the contact of two materials involves injection of electrons from the electrodes into the insulator and that is why tangent values are very low in the modeled environment. This process depends on the polarization conditions and the heat treatment as well^[39].

FEM simulation enabled to analyze proposed resonator configurations using CNC as piezoelectric layer and investigate the electrical performance of the composite and experimentally validate the approximate equations.

3.6. CNC thin-film composite cantilever modelling with FEM

In this section the previously introduced shear type CNC piezoelectric material is proposed to examine the energy harvesting performance of a cantilever arrangement of the CNC thin-film. The shear mode $d_{14}=d_{25}$ piezoelectric cantilever arrangement shown in Figure 3.8 schematically. One end of the cantilever is fixed to a table surface to vibrate along the vertical direction harmonically with a magnitude Y_0 at the formed angular frequency. On the other end a proof mass has been located, which is used to control the vibration and damping of the system. In the finite element calculation the vibrational energy has been converted to electrical energy. The dynamic modelling on the piezoelectric energy harvesting system is explained with mechanical parts and electrical output is evaluated from the finite element model. The mechanical modeling approach is simplified to a mass (M), spring (with constant K) and piston (with a damping coefficient C) mounted on a vibrating base (Fig.3.7)^[40].

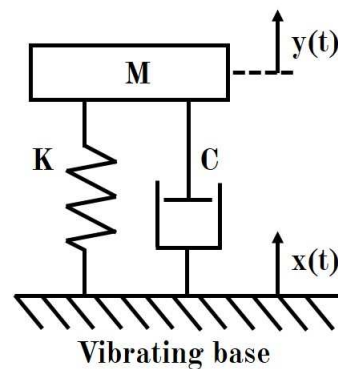


Figure 3.7. The cantilever single degree of freedom model.

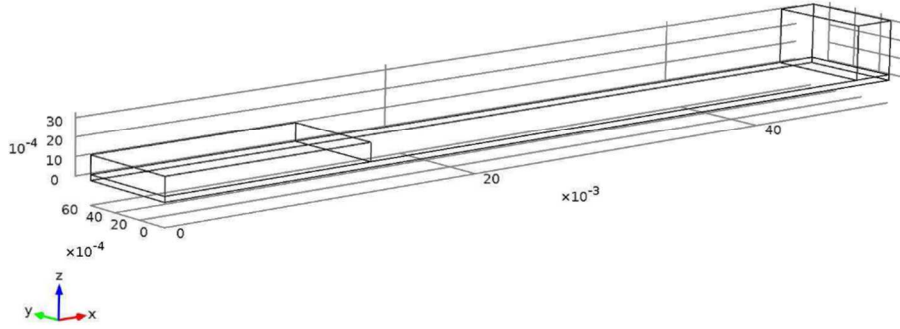


Figure 3.8. Shear mode piezoelectric cantilever schematic illustration.

The governing equation is:

$$\ddot{z} + 2\xi\omega_n\dot{z} + \omega_n^2z = -\ddot{y}^{[41]} \quad (3.12)$$

where $z = x(t) - y(t)$ is the relative motion between the mass and vibrating base and $\xi = C/2\sqrt{KM}$ is the damping ratio. For the piezoelectric cantilever in Fig. 3.8, the resonance angular frequency can be calculated as follows^[42]:

$$\omega_n = \sqrt{\frac{K}{M}} = \sqrt{\frac{9EI E_b I_b / (2EI(L-L_p)^3 + 5E_b I_b L_p^2(L-L_p))}{M_{tip} + (33/140)M_{beam}}} \quad (3.13)$$

where M_{tip} is the mass at the end of the cantilever and can be calculate as

$M_{tip} = r_b L b t_b + r_p L_b b_p t_p$ in which r_b, L, b, t_b and r_p, L_b, b_p, t_p are the mass density, length, width and thickness of the metal layer and the piezoelectric layer, respectively.

$E_b I_b = (1/12)(E_b/(1-\nu^2))b t_b^3 = (1/12)E_b b t_b^3$ and $EI = (1/3)E_B b(t_b^3 + 3t_b a^2 - 3t_b^2 a) + (1/3)E_p b_p(t_p^3 + 3t_p a^2 - 3t_p^2 a)$ are the flexural rigidity of

metal vibrating cantilever and piezoelectric/metal composite part, E_b is the Young's modulus, ν is the Poisson's ratio of the metal, E_p is the reciprocal of elastic compliance, and $a = (bE_b t_b^2 - b_p E_p t_p^2) / (2(bE_b t_b + b_p E_p t_p))$ the distance from the interface between piezoelectric layer and metal layer to the neutral axis of composite part.

The resonance frequency (eigenfrequency) of the piezoelectric cantilever can be calculated as 68.25 Hz according to Eq. (3.13), which is in good agreement with the FEM simulation 68.7 Hz (Fig. 3.9).

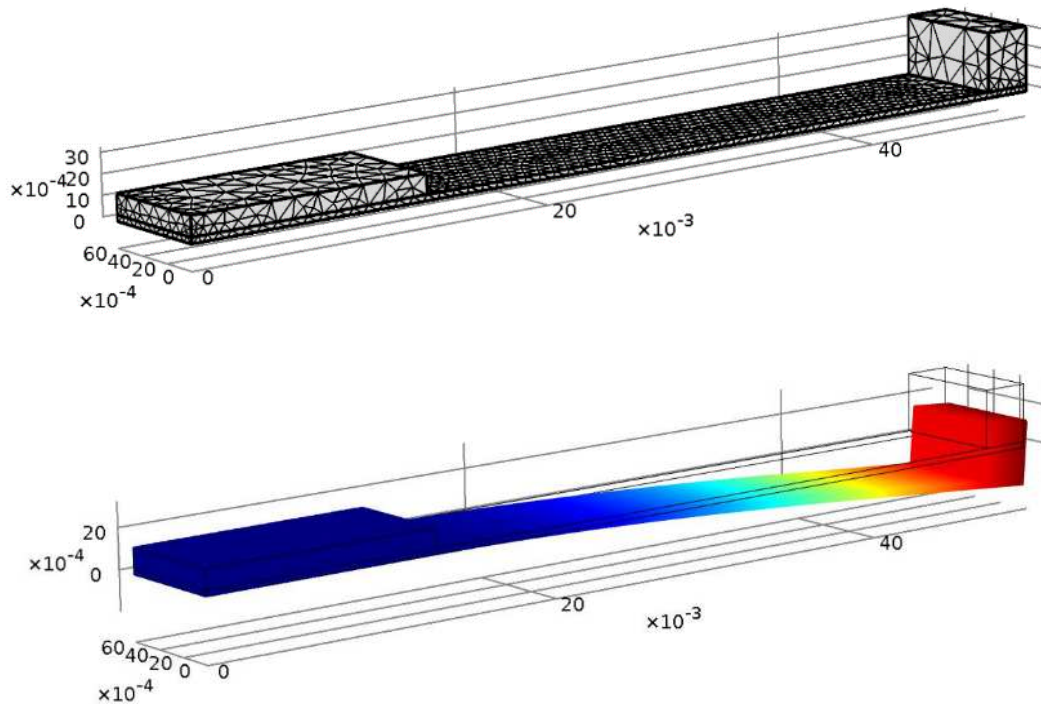


Figure 3.9. (a) The finite element mesh and (b) the modal deformation of shear mode piezoelectric cantilever.

The modeled CNC based piezoelectric cantilever bending sensor was developed and later it will be validate by real experimental arrangement. The model can properly describe the dynamic behavior of the sensor and estimate the output voltage.

3.7. Conclusion

In conclusion, we report the first experimental results showing that CNCs have a large piezoelectric response and found three different coefficient. In addition, the design and fabrication of ultrathin films of CNCs induce a high electromechanical actuation and strain which changes as a function of CNC alignment. Such structures can result in high mechano-electrical energy transfer. Thus, the electromechanical properties of ultrathin films of CNC can be considered in potential applications given their flexoelectric behavior, biodegradability, and renewability. Moreover, a bulk acoustic resonator and a piezoelectric cantilever are modelled using FEM analysis with the experimental and theoretical shear piezoelectric coefficient. The piezoelectric material and geometries of the proposed models can help us to predict ideal eigenfrequency product with maximum electrical outputs.

The results of the analytical and experimental works indicated the following conclusions:

1. It has been confirmed firstly that CNCs has a large piezoelectric response, $d_{25}=2.10\text{\AA}/\text{V}$.
2. It has been confirmed that the oriented CNCs thin films induce high electromechanical actuation and strain, which can results high mechano-electrical energy transfer.
3. It has been proved that the electromechanical properties of ultrathin films of CNCs and CNFs can be considered in potential micro-energy harvesting applications given their flexoelectric behavior, biodegradability, and renewability.
4. The developed finite element simulation procedure appears to adequately validate the piezoelectric cantilever structure using cellulose nanocrystals as a piezo layer on it.

3.8. References

1. H. Cheng, WW-EAP Newsletter 10(2) (2008) 5.
2. V. A. Bazhenov, Piezoelectric Properties of Woods 1961, Consultants Bureau, New York
3. E. Fukuda, History and Recent Progress in Piezoelectric Polymers 2000, IEEE transactions on Ultrasonics, Ferroelectrics, and Frequency Control, 47, 6, 1277.
4. J. Kim, N. Wang, Y. Chen, S. K. Lee, G. Y. Yun, Cellulose 14, (2007) 217.
5. M. T. R. Bhuiyan, N. Hirai, N. J. Sobue Wood Sci. 46 (2000) 431.
6. H. Maeda, E. J. Fukuda, Appl. Polym. Sci 33 (1987) 1187.
7. S. B. Lang, Nature (London) 212 (1996) 704.
8. Y. Nishiyama, S. Kuga, M. Wada, T. Okano, Macromolecules 30 (1997) 6395.
9. D. Bordel, J. L. Putaux, L. Heux, Langmuir 22 (2006) 4899.
10. Y. Habibi, T. Heim, R. J. Douillard, Polym. Sci. Pol. Phys. 46 (2008) 1430.
11. Y. Habibi, L. A. Lucian, O. J. Rojas, Chem. Rev. 110 (2010) 3479.
12. I. Hoeger, O. Velez, Y. Habibi, S. Kelley, O. J. Rojas, 239th ACS National Meeting, San Francisco, CA, 2010. March 21-25.
13. H. Asai, N. Watanabe, Biopolymers 15 (1976) 383.
14. C. D. Edgar, D. G. Gray, Cellulose 10 (2003) 299.
15. M. E. Leunissen, H. R. Vutukuri, A. van Blaaderen, Adv. Mater. 21 (2009) 3116.
16. J. Sugiyama, H. Chanzy, G. Maret, Macromolecules 25 (1992) 4232.
17. L. E. Helseth, Langmuir 21 (2005) 7276.
18. J. F. Revol, L. Godbout, X. M. Dong, D. G. Gray, H. Chanzy, G. Maret, Liq. Cryst. 16 (1994) 127.
19. F. Kimura, T. Kimura, M. Tamura, A. Hirai, M. Ikuno, F. Horii, Langmuir 21 (2005) 2034.
20. T. Ebeling, M. Paillet, R. Borsali, O. Diat, A. Dufresne, J. Y. Cavaille, H. Chanzy, Langmuir 15 (1999) 6123.
21. I. C. Hoeger, O. J. Rojas, K. Efimenko, O. D. Velez, S. Kelley, S. Soft Matter, 7 (2011) 1957.

22. F. J. Holler, D. A. Skoog, S. R. Crouch, Chapter 1. Principles of Instrumental Analysis (6th ed.) 2007, Cengage Learning. p. 9.
23. J. Kim, S. Yun, *Macromolecules* **39** (2006) 4202.
24. S. Yun, J. H. Li, Li. Y. Kim, J. J. Kim, *Appl. Phys.* **103** (2008) 083301-1.
25. W. S. Lee, J. H. Kim, J. Kim H. S. Kim, *Chinese Sci. Bull.* **54** (2009) 2703.
26. L. Csoka, I. Hoeger, P. Peralta, I. Peszlen, O. Rojas, *J Colloid Interf. Sci.* **363** (2011) 206.
27. M. Z. Birkholz, *Phys. B.* **96** (1995) 333.
28. R. H. Atalla, D. L. Van der Hart, *Science* **223** (1984) 283.
29. D. L. Van der Hart, R. H. Atalla, *Macromolecules* **17** (1984) 1465.
30. J. Sugiyama, T. Okano, H. Yamamoto, F. Horii, *Macromolecules* **23** (1990) 3196.
31. J. Sugiyama, J. V. Vuong, H. Chanzy, *Macromolecules* **24** (1991) 4168.
32. A. Sarko, R. Muggli, *Macromolecules* **7** (1974) 486.
33. K. M. Zhang, Y. P. Zhao, F. Q. He, D. Q. Liu, *Chinese J. Chem. Phys.* **30** (2007) 721.
34. F.L. Dri, L.G. Hector Jr., R.J. Moon, P.D. Zavattieri, *Cellulose* (2013) 2703.
35. Y. Nishiyama, P. Langan, H. Chanzy, *J Am Chem Soc* **124** (2002) 9074.
36. L. Csoka, D. Dudic, I. Petronijevic, C. Rozsa, K. Halasz, V. Djokovic, *Cellulose* **22** (2015) 779.
37. J.G. Simmons, *J Phys Chem Solids* **32**(8) (1971a) 1987.
38. J.G. Simmons, *J Phys Chem Solids* **32**(11) (1971b) 2581.
39. A. Thielen, J. Niezette, G. Feyder, J. Vanderschueren J., *J Phys Chem Solids* **57**(11) (1996) 1567.
40. L. Zhou, J. Sun, X.J. zheng, S.F. Deng, J.H. Zhao, S.T. Peng, Y. Zhang, X.Y. Wang, H.B. Cheng, *Sensor Actuat A-Phys* **179** (2012) 185.
41. T.H. Ng, W.H. Liao, *J Intel Mat Syst Str* **16** (2005) 785.
42. C.L. Sun, L.F. Quin, Li, Q.M. Wang, *J Intel Mat Syst Str* **20** (2009) 731.

Chapter 4

Preparation and characterization of bacterial cellulose thin films**4.1. Introduction**

Bacterial cellulose (BC), also known as microbial cellulose, is a promising natural polymer synthesized by certain bacteria such as *Gluconacetobacter xylinus*. Even though it is chemically identical to plant cellulose, its supramolecular structure and high purity cellulose content demonstrates unique properties such as high crystallinity (63-71 %), high water holding capacity (up to 200 times of its dry mass) and excellent mechanical strength. Young's modulus of BC sheets is in the range of 15-40 GPa, while that of a BC single fibril up to 114 GPa^[1,2]. BC binds large amounts of water - up to 99 wt% during its biosynthesis in the aqueous culture media^[3]. Several studies have focused on the utilization of BC as reinforcement material, in biomedical applications^[4,5] or cellulose based smart material devices^[6,7].

The isolation of cellulose nanoparticles without serious degradation, at low costs and using an environmentally friendly method is constantly being sought. Recently the application of ultrasound assisted extraction of plant polysaccharides^[8,9,10], ultrasound assisted delignification^[11,12], ultrasound assisted size reduction of cellulose^[13] or intensification of enzymatic hydrolysis^[14,15] has gained much interest.

Wang and Cheng^[16] examined the use of high intensity ultrasound to isolate fibrils from four cellulose sources: regenerated cellulose (lyocell), pure cellulose fiber, microcrystalline cellulose and pulp fiber. Wong et al.^[17] investigated the effect of ultrasound irradiation time on the depolymerization of plant and bacterial cellulose. Tischer et al.^[18] subjected BC pellicles to a high power ultrasonic treatment for 15, 30, 60 and 75 min; these were carried out in an ice bath for tissue engineering applications.

The aim of the present chapter was to examine the effect of two main ultrasound operating conditions, i.e the effect of temperature and distance of ultrasonic probe from the bottom of the beaker on morphological, structural and thermal properties of ultrasound defibrillated BC films. BC was previously pretreated in chemically mild conditions in order to: (i) maintain its native cellulose I structure, (ii) remove bacterial cell debris and (iii) to emphasize the subsequent ultrasound defibrillation treatment. The overall purpose of this research was to develop a method of obtaining highly crystalline and thermally more stable BC films suitable for energy harvesting devices, such as piezoelectric strain sensors. Energy harvesting has gained significant interest in the last couple of decades, where the main benefits are long-lasting operability of devices, no chemical disposal, cost savings, safety, and maintenance free, no charging points and flexibility. There are several vibrational power sources around us (photons, wind, mechano-luminescence crystals, thermal power and biochemical vibrations) where energy harvesting devices can show a good, alternative energy harvesting performance at micro-powering scale. In the coming years new electronic devices will be fabricated and the energy demand will decrease dramatically. Batteries has 34-90 $\mu\text{W}/\text{cm}^3/\text{yr}$ power, while ambient vibrations can generate 375 $\mu\text{W}/\text{cm}^3$ [19]. Collecting power from these ambient vibrations can meet with a practical level of power density for remote sensing application with a target 100 $\mu\text{W}/\text{cm}^3$ value[20]. Sensing in technological point of view or in environmental application tend to increase making our daily life more environmentally friendly. Energy harvesting nano and micro scale technologies can scavenge milliwatts from solar, vibrational, thermal and biological sources. Surface modified cellulose nanocrystals or nanofibrils, μ fibers can generate power, harvest energy as 10-12 $\mu\text{W}/\text{cm}^2$ magnitude in indoor environmental condition. **The aim of the present section is to introduce how we can fabricate chemically inert, well isolated cellulose nanofibrils from bacterial cellulose to increase its energy harvesting performance.**

Given the highlighted objectives, this chapter resulted one peer reviewed scientific publications in *Ultrasonics Sonochemistry* (a Q1 qualified journal) Vol. 28, pages 136-143 in 2016.

4.2. Materials and methods

4.2.1 Purification of nata de coco

Nata de coco cubes (PT. Cocomas, Indonesia) were washed and soaked in distilled water (water purification, WP) until the pH was neutral (pH 5-7) to remove the citric acid and other components of syrup added for preservation. In order to improve purity of BC, nata de coco was further purified by alkaline treatment to remove any remaining bacterial cell debris, microorganisms and other soluble polysaccharides. After being water purified, the nata de coco cubes were immersed in 2.5 wt% NaOH (6×10^{-3} M) overnight. This process will be hereafter referred as one step purification (OSP). Another sample was prepared in the same way and successively treated with 2.5 wt% NaOCl (3.4×10^{-3} M); hereafter referred to as two step purification (TSP). OSP and TSP treatments were carried out by adopting the methodology as reported by Gea et al^[21]. A third sample was prepared by warming nata de coco in 0.01 M NaOH at 70°C for 2 h under continuous stirring; this will be called as 0.01 M NaOH purification.

Subsequently, nata de coco cubes were rinsed under distilled water at room temperature (RT) until the pH of the water became neutral. Once neutral pH was reached, BC was mechanically ground and homogenized in a 400 W blender for 10 min (medium speed, 5 times x 2 min with 5 min intervals). Afterwards, blended BC was poured into confined space silicon trays, and dried via solvent evaporation in an oven at 50 °C, for two to three days.

4.2.2 Ultrasonication of bacterial cellulose films

After drying, the BC films were cut and were redispersed (0.1 % w/w, immersed in 80 mL distilled water) and subjected to further grinding, this time with a hand blender for 20 s, prior to ultrasonication. Sonication was directly applied at low frequency (20 kHz) using an ultrasonic horn (Tesla 150 WS) with a tip diameter of 18 mm immersed in the suspension. HIUS treatment of BC performed using three levels of temperature; room temperature or no water bath (NoW), cold water bath (CW) and ice water bath (IW) and two levels of ultrasonic probe distance from the bottom of a

beaker; 1 cm and 4 cm respectively to evaluate the effect of cavitation active zones, local circulation and ultrasonic intensity distribution on BC microfibrils. The ultrasonic probe was placed close to the surface (4 cm distance) and close to the bottom (1 cm distance) of a 100 mL cylindrical beaker. A 7.4 cm distance (1 wavelength of ultrasound in water) was not possible to be examined, owing to the height of the beaker. When cold water bath was used for cooling, the temperature was about 12 ± 2 °C, whereas it was around 5 ± 1 °C when ice bath was used. Frequency (20 kHz), amplitude (20 microns), power ($25\text{W}/\text{cm}^2$) and ultrasonication time (30 min) were kept constant.

4.2.3 Preparation of bacterial cellulose films

Resulting ultrasound colloid dispersions were left to stand overnight. Thereafter, the liquid supernatant phase (around 40 ml) was collected from ultrasound treated BC, poured again into silicon trays and dried similarly through solvent evaporation, for a second time. The dried, ultrasound reconstituted BC films were carefully removed and stored in plastic bags until further analysis. Due to the drying method, BC micro/nanofibrils were randomly oriented, which assumes isotropic characteristics for the BC film.

4.3. Methods

Field Emission Scanning Electron Microscopy (FE-SEM)

FE-SEM micrographs were obtained using a Zeiss ULTRA Plus (Oberkochen, Germany) instrument at an acceleration voltages of 1 and 2 kV. The suspensions were filtered through a gilded PC membrane and dried for 1 h at room temperature. All samples were coated with a highly conductive film of gold by Bal-Tec SCD 500.

4.3.1 Atomic Force Microscopy (AFM)

AFM experiments were performed using a MultiMode atomic force microscopy 8 with a Nanoscope Veeco V controller (Bruker Nano Surfaces, Santa Barbara, CA, USA) instrument. Small cut pieces of dried BC films were placed on magnetic slides and the scans were obtained in tapping mode

using a V-shape Silicon Nitride cantilever. Prior to the measurements, the tip radius and geometry of the tip were calculated. Two repetitions of imaging ($5 \times 5 \mu\text{m}$ and $1 \times 1 \mu\text{m}$) were carried out. These experiments were implemented in an environment with constant relative humidity and temperature. Width was measured by image analysis using ImageJ software (ImageJ 1.46, National Institute of Health (NIH), USA).

4.3.2 Fourier Transform Infrared Spectroscopy (FT-IR)

FTIR spectra of the BC films were obtained using a Jasco FT/IR6300 equipped with an ATR PRO 470-H spectrometer. A total of 50 cumulative scans were taken per sample with a resolution of 4 cm^{-1} , in the frequency range of $4000\text{--}400 \text{ cm}^{-1}$, in absorbance mode. ATR correction was applied in each measurement.

4.3.3 X-ray Powder Diffraction (XRD)

The X-ray diffraction patterns were recorded at room temperature in the $5\text{--}80^\circ 2\theta$ range using an MPD Pro Panalytical diffractometer equipped with an Xcelerator linear detector. Cu-K (1.54056 \AA) radiation was used with the 0.016° recording step and the 1000 s per step counting time. The samples were powdered before the analysis.

XRD peak height method, developed by Segal and coworkers [20], was used to determine the crystallinity index (Cr.I) by the following equation (Eq.4.1)

$$Cr.I = \frac{I_{200} - I_{am}}{I_{200}} 100 \quad (4.1)$$

where I_{200} is the peak intensity at the (200) ($2\theta \approx 22.5^\circ$) plane, and I_{am} is the minimum intensity (amorphous scatter) at the valley between (200) and (110) peaks ($2\theta \approx 18^\circ$).

The interplanar distances of the crystallites (d-spacings) were calculated with Bragg's law,

$$\lambda = 2d \sin\theta \quad (4.2)$$

where λ is the wavelength of the X-rays, d is the spacing between the crystal planes in the atomic lattice, and θ is the Bragg angle between the incident ray and the scattering planes^[23].

The crystallite sizes at d_1 , d_2 and d_3 , the three main peaks respectively, were determined using the Scherrer equation^[24]:

$$Cr.S. = \frac{0.9\lambda}{H_{hkl} \cos\theta_{hkl}} \quad (4.3)$$

where $Cr.S.$ is the crystallite size, λ is the wavelength of incident X-rays, H_{hkl} is the full-width at half-maximum (FWHM) and θ_{hkl} is the Bragg angle at the corresponding lattice plane.

4.3.4 Thermal analysis

Thermal analysis techniques, thermogravimetric analysis (TGA) and differential scanning calorimetry (DSC) were used to measure the thermal stability behavior of BC films. Thermogravimetric (TG) data were acquired between 0 and 500 °C using a Perkin Elmer Diamond thermal analyzer under nitrogen purging gas (100 cm³min⁻¹) at a heating rate of 2 °C min⁻¹. Differential scanning calorimetry (DSC) analysis was carried out on a Netsch DSC204 instrument under nitrogen purging gas (30 cm³min⁻¹) at a heating/cooling rate of 2 K min⁻¹. Temperature and enthalpy were calibrated using the melting transition of standard materials (Hg, In, Sn).

4.4. Results and Discussion

4.4.1 Morphological analysis

FE-SEM images, of dried films after the purification treatments and prior to ultrasonication are shown in Fig 4.1. The typical network structure attributed to native BC was presented in all purified samples. The surface structure of BC is characterized by a 3-D fibrous ultrafine network of well-arranged nanofibrils, stabilized by the hydrogen bonds existing in cellulose units^[25-27].

From Fig. 4.1a, it can be seen that, WP method was only adequate to remove the syrups contained within nata de coco package. Bacterial cell debris and other contaminants were slightly removed after the OSP purification treatment, as shown in Fig. 4.1b. The successive treatment with 2.5 wt% NaOCl in TSP caused the removal of a higher amount BC debris (Fig. 4.1c). However, their existence was still visible. From Fig. 4.1d, it is clear that, BC treated in 0.01 M NaOH at 70 °C for 2 h under continuous stirring, displayed the most ideal results. On their surface there were almost no bacterial skeletons and only BC nanofibrils had remained. High resolution FE-SEM images of non-ultrasound water purified BC samples and 0.01 M NaOH purified BC samples after ultrasound treatment are shown in Fig. 4.1e and Fig. 4.1f. Their mean width was found to be 23.16 and 11.15 nm respectively.

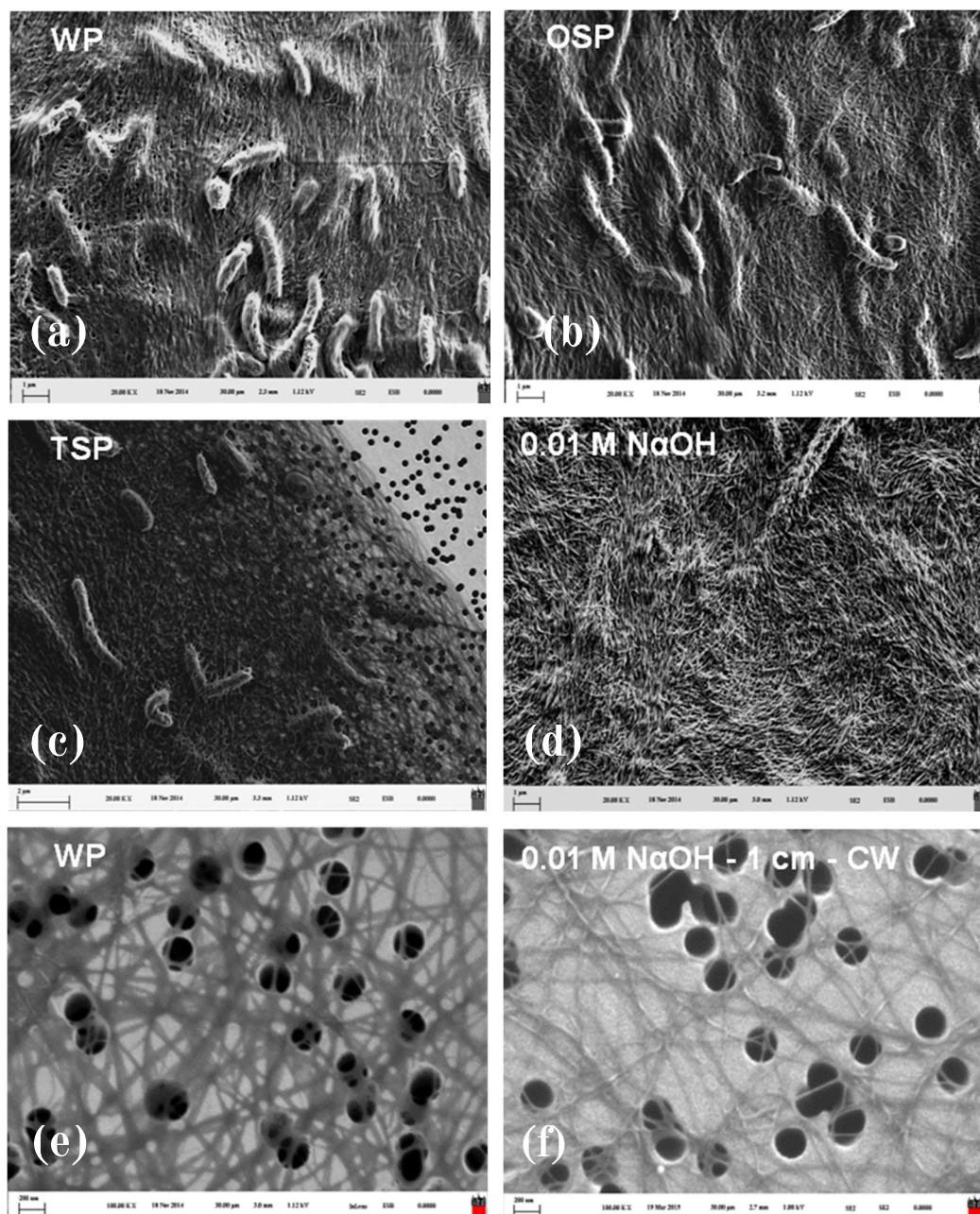


Figure 4.1. FE-SEM micrographs of (a) WP (1 μ m), (b) OSP (1 μ m), (c) TSP (1 μ m), (d) 0.01M NaOH purified (1 μ m), (e) WP before ultrasound (200 nm) and (f) ultrasonicated 0.01 M NaOH - 1 cm - CW (200 nm) BC samples

4.4.2 Atomic Force Microscopy (AFM)

The surface topography of each BC sample was further characterized by AFM (Fig. 4.2). The dense and aggregated typical BC structure on the dried films, is more apparent by AFM microscopy.

Besides, agglomeration of BC microfibrils is also a result of the drying process. Pa'e et al.^[28] investigated the effect of different methods on the crystallinity, swelling ability and tensile properties of nata de coco. The surfaces of oven dried BC films were constituted of numerous randomly oriented and overlapped fibrils producing an aggregated web structure. During water evaporation, the capillary forces among cellulose fibrils increased, their distance became much shorter and strong molecular contact was achieved, resulting in solid, bulk films. Similar observations, as in FE-SEM images were observed in the width of cellulose microfibrils.

Although alkali purification treatments were suitable to remove bacterial debris, they were not appropriate to form suitable films for nanocellulose applications. Ultrasound process altered the microfibrillar arrangement of BC, leading to new films with different nanostructure organization, as shown in Fig. 4.3. Similar films were obtained after drying the supernatant phase of ultrasound colloid samples at 50 °C, independently of the purification method.

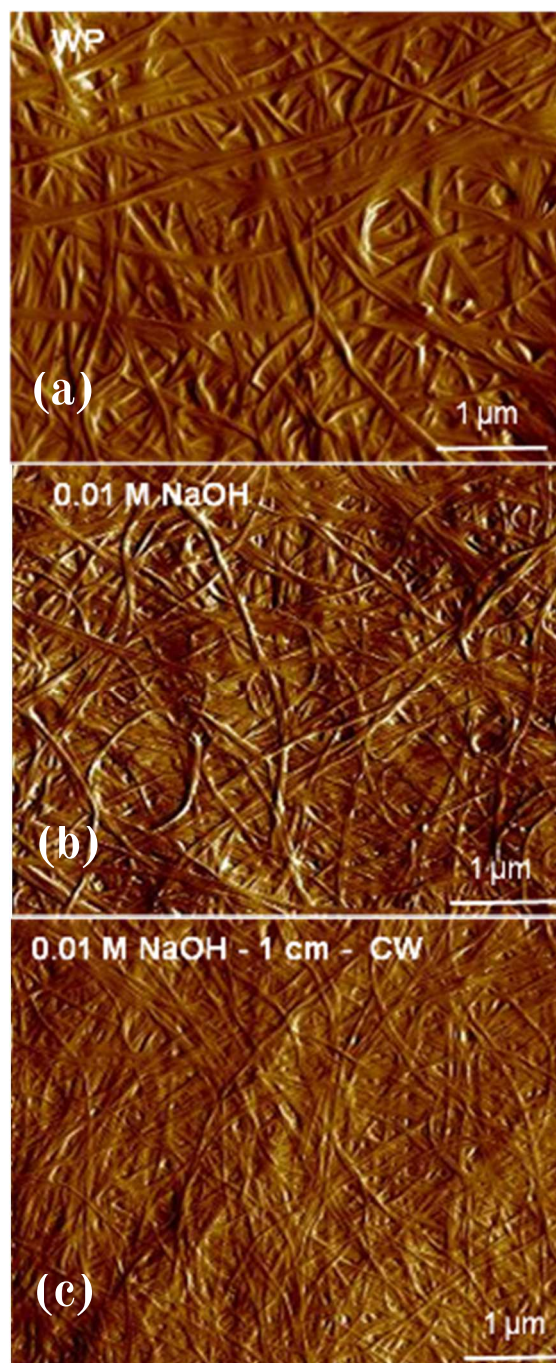


Figure 4.2. AFM images of (a) WP, (b) 0.01 M NaOH purified and (c) ultrasonicated 0.01 M NaOH - 1 cm - CW BC samples

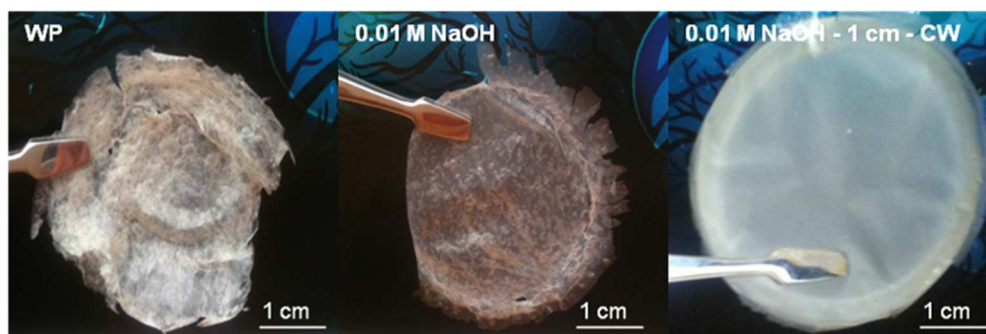


Figure 4.3. Macroscopic images of (a) WP, (b) 0.01 M NaOH purified and (c) ultrasonicated 0.01 M NaOH - 1 cm - CW BC dried films

4.4.3 Fourier Transform Infrared Spectroscopy (FT-IR)

0.01 M NaOH treatment, was chosen for further research as the most favourable purification method. The influence of ultrasound on 0.01 M NaOH purified BC was first evaluated by FT-IR spectroscopy. For a more comprehensive and qualitative analysis and investigation of the FT-IR spectra, the FT-IR spectra were divided in two regions, 4000-2600 cm^{-1} and 1800-800 cm^{-1} (Fig. 4.4).

Within the absorbance range of 3600 to 3000 cm^{-1} , a consistent strong and sharp peak (3340 cm^{-1}) typical to cellulose I intramolecular hydrogen bond was observed in all treatments. In purified treated samples the C-H stretching band existed in 2900 cm^{-1} , which is also assigned to cellulose I. However, after ultrasonication the absorbance in this region became broader and alkaline treated samples displayed two peaks.

The “fingerprint” region 1800-800 cm^{-1} is more complicated. This region contains the largest number of spectral differences, which permits the identification of any structural changes within cellulose samples. In all FT-IR spectra, the following characteristic bands were observed: 1428 cm^{-1} (CH_2 symmetric bending), 1330 cm^{-1} (- OH in plane bending), 1316 cm^{-1} (CH_2 wagging at C-6), 1160 cm^{-1} (C-O-C asymmetric stretching), 1111 cm^{-1} (ring asymmetric stretching), 1058 cm^{-1} (C-O stretching), 1030 cm^{-1} (stretching C-O) and 986 cm^{-1} (C-O valence vibration at C-6). This spectra behaviour is assigned to native cellulose.

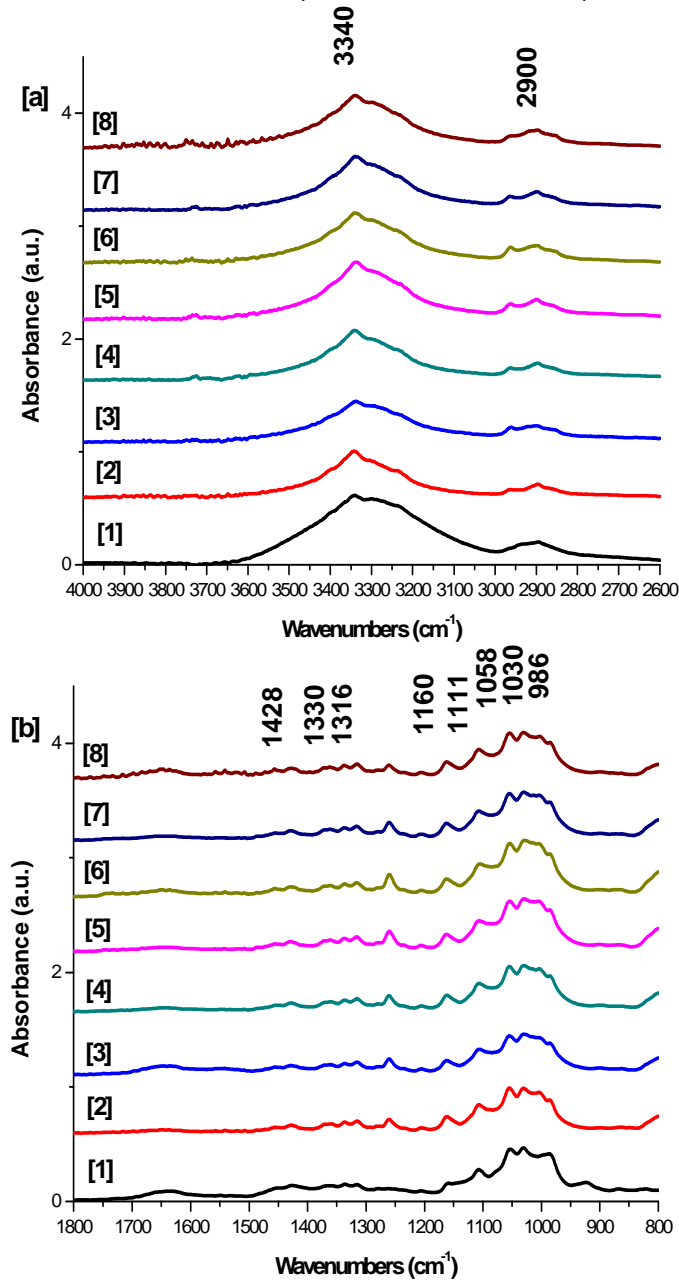


Figure 4.4. Comparative FT-IR spectra of the (a) 3800-2600 cm⁻¹ region and (b) 1800-800 cm⁻¹ region of BC samples: [1] WP no ultrasound, [2] 0.01 M NaOH purification no ultrasound, [3] 0.01 M NaOH - 1 cm - NoW, [4] 0.01 M NaOH - 1 cm - CW, [5] 0.01 M NaOH - 1cm - IW, [6] 0.01 M NaOH - 4 cm - NoW, [7] 0.01 M NaOH - 4 cm - CW, [8] 0.01 M NaOH - 4 cm - IW

The most notable changes in cellulose occur at 1430 cm^{-1} , 1162 cm^{-1} , 1111 cm^{-1} , 986 cm^{-1} and 893 cm^{-1} absorption bands. In these bands the crystalline cellulose I spectrum differs significantly in relation to cellulose II and amorphous cellulose [27,28]. Furthermore, there is no indication of the following absorption bands, 1376 and 1278 cm^{-1} , assigned mainly to crystalline cellulose II and amorphous cellulose^[31].

The Lateral Order Index (LOI) and Total Crystallinity Index (TCI), proposed by Nelson and O'Connor^[32,33] and O'Connor^[34] respectively, were used to study the infrared crystallinity changes of cellulose samples. The so-called hydrogen bond intensity (HBI), is closely related to OH region and the intermolecular and/or intramolecular hydrogen bonding network, which sensitively follows the physical and structural changes of cellulose during ultrasound treatment^[30,35-36]. The results of the infrared crystallinity ratios (TCI, LOI) and hydrogen bond intensity (HBI) are shown in Table 4.1.

It should be noted that even though this method is simple and fast, it provides relative crystallinity index (Cr.I.) values only, owing to the fact that the spectrum always contains contributions from both crystalline and amorphous regions [35]. TCI is proportional to the crystallinity degree of cellulose, while LOI is related to the overall degree of order in cellulose^[38]. Poletto et al. report that cellulose samples with higher TCI, LOI and HBI might demonstrate higher crystallinity. On the contrary, Carrillo et al.^[29] mentioned that higher crystallinity, in the case of regenerated cellulose, was indicated when TCI values were increased and LOI values were decreased.

In this study, it had been attempt to investigate the possibility of empirically estimating the crystallinity of BC relying on LOI, TCI and HBI values. In accordance with the results, a combination of higher TCI and lower LOI indices was selected for comparison among ultrasound treated 0.01 M NaOH purified BC samples, as reported in Carillo et al. The other option, i.e. the combination of higher TCI and LOI values was preferred among the different BC purification treatments.

The following ultrasound operating conditions of 0.01 M NaOH purified BC samples were chosen for further characterizations with XRD, TGA and DSC techniques: (i) 1 cm distance of the ultrasonic probe - no water bath (1 cm - NoW), (ii) 1 cm distance of the ultrasonic probe - cold water bath (1 cm - CW) and (iii) 4 cm distance of the ultrasonic probe - cold water bath

(4 cm – CW). No ultrasonicated 0.01 M NaOH purified BC samples were also examined as control.

Table 4.1. Determined lateral order (LOI), total crystallinity (TCI) infrared crystallinity indices and hydrogen bond intensity (HBI) values.

Treatment	TCI	LOI	HBI
	A_{1372}/A_{2900}	A_{1430}/A_{898}	A_{3308}/A_{1330}
WP - No ultrasound	0.67	0.85	2.97
0.01 M NaOH - No ultrasound	0.73	1.32	3.80
0.01 M NaOH - 1 cm - NoW	0.76	1.22	2.81
0.01 M NaOH - 1 cm - CW	0.75	1.21	3.35
0.01 M NaOH - 1 cm - IW	0.69	1.23	3.38
0.01 M NaOH - 4 cm - NoW	0.62	1.30	3.64
0.01 M NaOH - 4 cm - CW	0.63	1.30	3.89
0.01 M NaOH - 4 cm - IW	0.66	1.40	3.72

XRD results showed that in water purified and the highly crystalline 0.01 M NaOH purified BC, Cr.I. was almost identical. This could be a possible explanation of obtaining similar TCI and LOI values after ultrasonication. In contrary, there were observed changes in these values among purification treatments and in ultrasonicated OSP and TSP bacterial cellulose samples. Cr.I was notably increased after application of ultrasound in OSP and TSP bacterial cellulose.

4.4.4 X-ray diffraction analysis (XRD)

The X-ray diffraction patterns of ultrasound-treated BC obtained from 0.01 M NaOH purified nata de coco are presented in Fig. 4.5. Diffractograms displayed three main characteristic peaks assigned to cellulose I in X-ray diffractions, and these are located at approximately $2\theta = 14^\circ$, 16° and 22° corresponding to $1\bar{1}0$ (d_1 spacing), 110 (d_2 spacing) and 200 (d_3 spacing) crystallographic planes respectively. The diffractogram peak located at around $2\theta = 35^\circ$, corresponds to 040 crystallographic plane^[39,40].

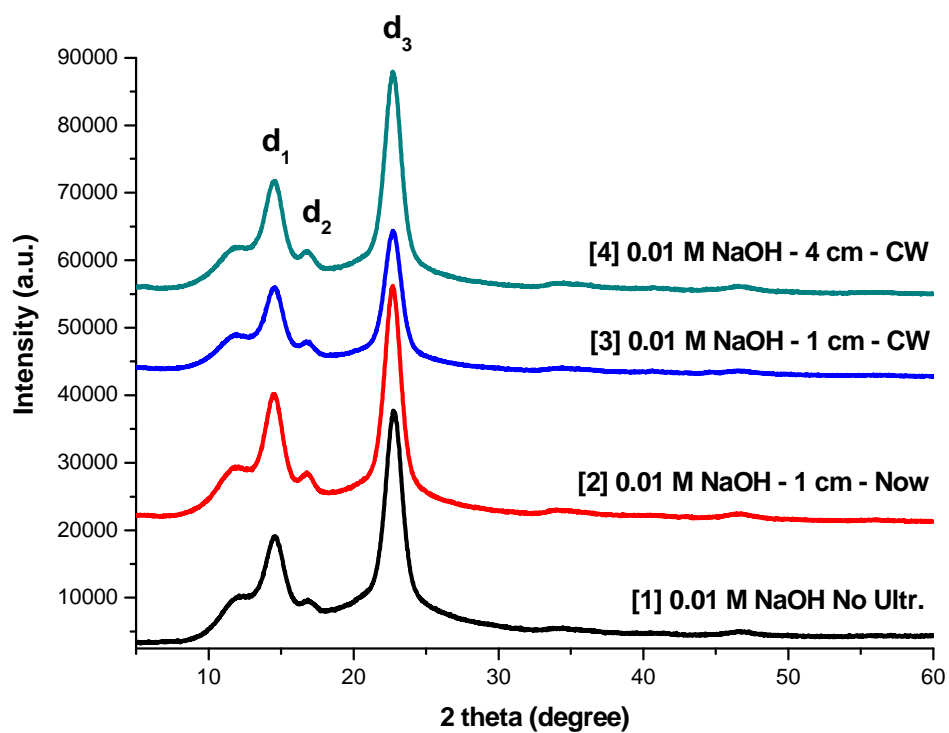


Figure 4.5. X-ray diffraction patterns of [1] 0.01 M NaOH purification no ultrasound, [2] 0.01 M NaOH - 1 cm - NoW, [3] 0.01 M NaOH - 1 cm - CW and [4] 0.01 M NaOH - 4 cm - CW BC samples.

The X-ray diffractograms, showed no change in peak intensities located at the crystallographic plane reflections, indicating no transformation of cellulose I into cellulose II allomorph due to ultrasonication. d-spacing values, crystallite sizes of the three characteristic planes, as well as their crystallinity index (Cr.I) calculated from X-ray diffractograms are given in Table 4.2.

Table 4.2. XRD d-spacings, peak intensities, crystallite sizes at 2θ angles and Cr. I. of 0.01 M NaOH BC under the investigated ultrasound operating conditions.

Treatment	d spacings (nm)			Cr. size (nm)			Cr. I (%)
	d1	d2	d3	d1	d2	d3	
0.01 M NaOH - No ultrasound	0.60	0.52	0.39	5.45	5.47	5.52	77.7 8
0.01 M NaOH - 1 cm - NoW	0.60	0.53	0.39	4.88	5.43	6.1	80.4 6
0.01 M NaOH - 1 cm - CW	0.60	0.52	0.39	4.71	5.19	5.8	77.6 2
0.01 M NaOH - 4 cm - CW	0.60	0.53	0.39	5.55	5.57	5.6	81.7 0

Results demonstrated no changes in the interplanar distances (d-spacings) among untreated and ultrasound treated BC samples. d-spacing values are in accordance with Amin et al.^[41] who investigated the properties of acid and mechanically treated, spray-dried BC obtained from nata de coco. Nevertheless, the crystallite sizes in $1\bar{1}0$ (d_1 spacing), 110 (d_2 spacing) and 200 (d_3 spacing) lattice planes displayed shifted values, influenced by the different ultrasound operating conditions. These results indicate that ultrasound treatment resulted in changes to the crystalline shape of BC microfibrils.

4.4.5 Thermogravimetric analysis (TGA)

The thermogravimetric (TGA) and derivative thermogravimetric (dTGA) curves of ultrasound treated 0.01 M NaOH alkaline-purified BC samples have been shown in Fig. 4.6.

Thermal degradation of BC includes depolymerisation, dehydration and decomposition of glycosic units, and subsequent oxidation leading to the formation of a charred residue. To examine the thermal degradation behaviour, the onset thermal degradation temperature (T_d) was taken at 10% weight loss. The thermal decomposition of cellulose known as maximum degradation temperature (T_{dmax}), was determined from dTGA curves.

The degradation patterns in terms of shape and temperature seems to be quite similar for ultrasound-treated samples. All samples showed a slight weight loss at low temperatures (<100 °C) corresponding to evaporation of absorbed water. The T_d temperature, were observed at 285 °C, 309 °C, 316 °C and 312 °C for 0.01 M NaOH purified, 0.01 M NaOH - 1 cm - NoW, 0.01 M NaOH - 1 cm - CW, 0.01 M NaOH - 4 cm - CW BC samples respectively. The dTGA peak accounting for T_{dmax} temperature of cellulose, were observed at around 368 °C, 376 °C, 374 °C and 374 °C respectively.

The onset temperature and the maximum degradation temperature of simply 0.01 M NaOH purified BC were both lower than that of the ultrasound treated. The improved thermal stability of ultrasonicated BC films is useful for potential medical and energy harvesting applications.

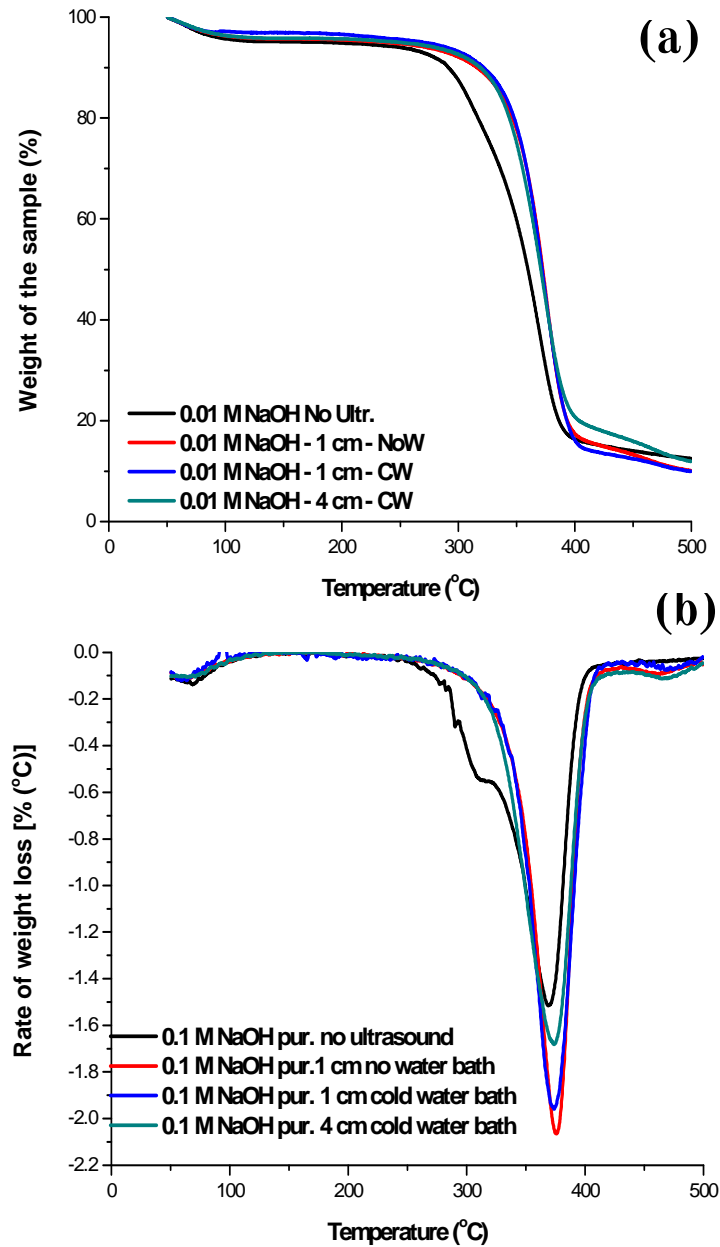


Figure 4.6. (a) TGA and (b) dTGA curves of 0.01 M NaOH purified BC under the examined ultrasound operating conditions

4.4.6 Differential Scanning Calorimetry (DSC)

DSC thermograms of 0.01 M NaOH alkaline-treated BC samples obtained after the considered ultrasound operating conditions are shown in Fig. 4.7.

The thermal behavior presented in all samples is related to monotropic solid-to-solid transition, which is an endothermic reaction and frequently occurs in organic compounds, like cellulose. This kind of feature was possible to be observed because of the low DSC heating rate (2 K min^{-1}) and indicated the slow transition and rearrangement of amorphous regions to a stable crystalline phase. A possible explanation is given by Tischer et al.^[18]. They claim that ultrasound energy transferred through shearing and cavitation phenomena to the glucan chains, promoted the conversion of amorphous material into crystalline material.

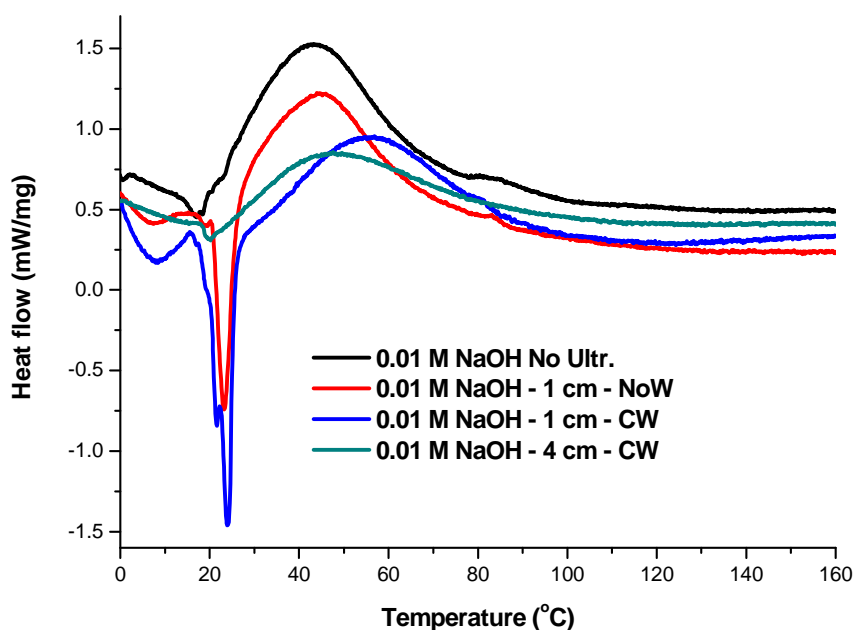


Figure 4.7. DSC curves of 0.01 M NaOH purified BC under the investigated ultrasound operating conditions.

4.4.7 Effect of alkaline treatment

Even though BC is free from hemicelluloses and lignin contaminants, the ferment broth contains other impurities such as BC debris and the remaining culture medium. The most suitable purification methods for the removal of the mentioned impurities are distilled water, sodium hydroxide and sodium hypochlorite solutions, or organic acids like acetic acids^[42,43].

The most common purification BC method is in aqueous solutions of 0.1 M NaOH. However, in this study it was found that 0.01 M NaOH at 70 °C for 2 h under continuous stirring was capable enough of removing BC debris. Warm temperature conditions at 70 °C allowed better alkali penetration into the inner parts of nata de coco cubes and BC aggregated microfibrils than by carrying out at ambient temperatures. It is well known that proteins and nucleic acids can be hydrolyzed with alkaline solutions at warm temperatures.

Alkaline treatments, even at these low concentrations, can cause a weak to very low swelling on BC samples^[44,45]. It is assumed, that swelling increased the contact surface area between solid and liquid phases and assisted in accelerating the mass transfer and shear forces produced during ultrasound, causing friction of BC microfibrils, thus crystallite size changes took place.

4.4.8 Effect of ultrasound operating conditions

Ultrasound function, although seems to be simple, actually is quite complex. Ultrasonication is influenced by many operating parameters and even slight changes could attribute to significant variations in ultrasound efficiency. Some parameters, such as geometry of ultrasonic horn, operating frequency, ultrasound energy distribution are not easy to change or to control.

For this study, a frequency of 20 kHz was considered as the optimum ultrasound frequency since it was found to be effective for extraction of plant contents^[9]. The intensity of ultrasound, which is proportional to the amplitude of vibration^[46] was kept constant at 20 microns. Water due to its susceptible action to formation of hydroxyl radicals during cavitation was used as solvent.

On the contrary, other parameters can be investigated in order of achieving the most suitable ultrasound conditions. Considering the reaction of a cavitation process, bulk operating conditions such as time, ultrasonic power, distance of ultrasonic probe and temperature are crucial factors, which often interact with each other.

It was found that as ultrasonication time was increased, faster cellulose degradation rate was observed and crystallinity of cellulose was also decreased^[13]. Moreover, ultrasonic power influences the number of cavitation bubbles formed, their lifetime and the generated cavitation intensity. On account of preliminary research the selected operating time and power were 30 min and around 25 W/cm² respectively, to attain defibrillation and liberation of nanofibrils, but which simultaneously avoids the possible cellulose decomposition.

Acoustic cavitation phenomenon is a function of vapor pressure and temperature. High solvent temperatures are more desirable to disrupt strong interaction forces such as van der Waals, hydrogen bonds and dipole attraction between the solute molecules and solute-matrix. In contrast at lower temperatures depending on ultrasound intensity, vapor pressure is less intense, a large number of bubbles collapse more violently with smaller radius, higher internal temperature is reached and cavitation activity become stronger^[46].

The decreasing bath temperature influenced the temperature of BC aqueous dispersions, so the ultrasound intensity and cavitation efficiency as well. In the absence of water cooling, rapidly high temperature was obtained into the BC aqueous colloid biphasic system. As a result, isolation of BC micro and nanofibrils^[47] could be amplified, yet ultrasound energy conversion efficiency was promptly reduced. In ice water bath, liquid dispersion attained the lowest temperature. Likelihood, acquired temperature was not sufficient enough of breaking van der Waals and hydrogen bond forces of BC microfibrils. It is believed that moderate temperature conditions demonstrated in cold water bath treatment is the most favourable option.

Ultrasound intensity and the pressure field are not uniformly distributed in the reactor. Highest intensity is found only close to tip and then rapidly decreases mostly axially due to different damping forces, but also radially from the ultrasonic probe. Besides it depends on tip diameter, the formation of sound waves and position of probe into the liquid level^[48]. The distance of

probe from the bottom of the container as the depth of probe immersion, affect the number and distribution of cavitation zones and local turbulence circulation displacement.

By minimizing dead zone areas below ultrasonic probe and the wall of the beaker, at 1 cm distance, a maximum contact degree between BC and mass transfer forces of cavitation zones could occur. Numerical simulations exhibited rather robust circulation and two active areas at 4 cm distance, instead of one zone at 1 cm distance. It has to be mentioned, that characterization techniques on the selected BC samples did not show any essential differences between the applied distances. Based on subjective observations and impression of results, it is thought that treatment at 1 cm distance resulted more preferable films compared to that of treatment at 4 cm distance.

4.5. Conclusions

The current chapter examined the feasibility of ultrasound treatment in the separation of BC nanofibrils and the fabrication of thin BC films. High intensity ultrasound, when it was applied in purified BC colloid dispersion, had a considerable impact on morphology and supramolecular properties of cellulose. The most favorable results were regarded to be obtained in 0.01 M NaOH purified BC samples combined with 1 cm distance placement of the ultrasonic probe from the bottom of the beaker, submitted to cold water bath cooling. The supernatant phase of the ultrasound treated colloid was subjected to solvent evaporation in order to obtain films with the finest BC nanoparticles.

Cellulose-based energy harvesting devices, such as piezoelectric sensors, are an emerging field of research. Further investigations in alignment of BC fibrils, cellulose reactivity, piezoelectric film dimensions and fabrication of piezoelectric cantilever, modeling of ultrasonication and piezoelectric effect should be considered. However, the developed method resulted in the formation of self-assembled, highly crystalline thin films, which could be useful in nanotechnology applications where the utilization of such films is important. One of that first, preliminary results is shown in the following image. High-power ultrasound liberated bacterial cellulose nanofibrils has been deposited on an alumina layer and tested in a cantilever mode to prove

the piezoelectric response from the film. It can be seen from the image that during the damping of the resonating cantilever (mechanical excitation), different magnitude voltage peaks raised. This clearly indicate the direct piezoelectric effect of the fabricated nanofibrillated cellulose film.

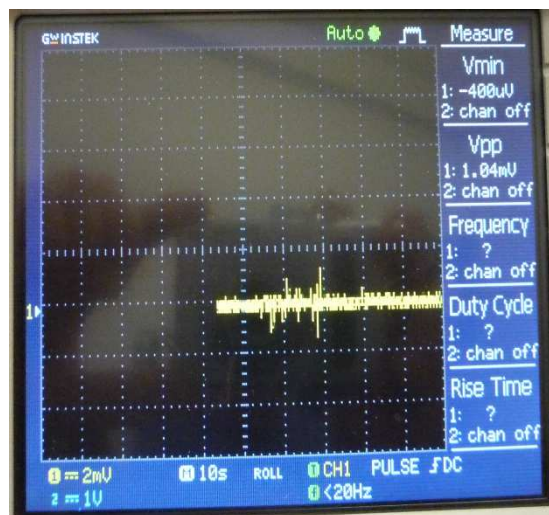


Figure 4.8. Electrical signal was obtained from high-power ultrasound liberated cellulose nanofibrils in a cantilever arrangement under mechanical excitation.

Our results demonstrated that ultrasonication was an advantageous technique of isolating cellulose nanofibrils, while concurrently enhanced their crystallinity. This mild way of mechanical treatment facilitated the separation of inherent aggregated, purified BC microfibrils, altered the size and shape of BC crystallites and introduced a new reformed homogeneous, well-redispersed film. Variations in TCI, LOI and HBI index values imply that ultrasound influenced the hydrophilic behavior and cellulose surface accessibility and reactivity of the obtained BC films.

4.6. References

1. R. Khajavi, J.E. Esfahani, M. Sattari, *International Journal of Polymeric materials* 60 (2011) 1178-1192.
2. Y.-C. Hsieh, H. Yano, M. Nogi, S. J. Eichhorn, *Cellulose* (2008) 507-513.
3. K. Gelin, A. Bodin, P. Gatenholm, A. Mihranyan, K. Edwards, M. Strømm, *Polymer* 48 (2007) 7623-7631.
4. P. Gatenholm, D. Klemm, *MRS Bulletin* 35 (2010) 208-213.
5. L. Fu, Y. Zhang, G. Yang, *Carbohydrate Polymers* 92 (2013) 1432-1442.
6. A. Baptista, I. Ferreira, J. Borges, , *InTech* 2013. pp. 67-82.
7. S. Ummartyotin, J. Juntaro, M. Sain, H. Manuspiya, *Industrial Crops and Products* 35 (2012) 92-97.
8. A. Ebringerová, Z. Hromádková, *Cent. Eur. J. Chem.* (2010) 243-257.
9. S.R. Shirsath, S.H. Sonawane, P.R. Gogate, *Chemical Engineering and Processing* 53 (2012) 10-23.
10. I. Alzorqi, S. Manickam, *AIChE Journal* 61 (2015) 1483-1491.
11. A. Iskalieva, B.M. Yimmou, P.R. Gogate, M. Horvath, P.G. Horvath, L. Csoka. *Ultrasonics Sonochemistry* 19 (2012) 984-993.
12. P.B. Subhedar, P.R. Gogate, *Ultrasonics Sonochemistry* 21 (2014) 216-225.
13. DV Pinjari, A.B. Pandit, *Ultrasonics Sonochemistry* 17 (2010) 845-852.
14. P.B. Subhedar, P.R. Gogate, *Ind. Eng. Chem. Res.* 52 (2013) 11816-11828.
15. O.E. Szabó, E. Csiszár, *Carbohydrate Polymers* 98 (2013) 1483-1489.
16. S. Wang, Q. Cheng, Part 1: Process Optimization, *Journal of Applied Polymer Science* 113 (2009) 1270-1275.
17. S-S. Wong, S. Kasapis, Y.M. Tan, *Carbohydrate Polymers* 77 (2009) 280-287.
18. P.C.S.F. Tischer, M.R. Sierakowski, H. Westfahl Jr., C.A. Tischer, *Biomacromolecules* 11 (2010) 1217-1224.
19. S. Roundy, E.S. Leland, J. Baker, E. Carleton, E. Reilly, E. Lai, B. Otis, J.M. Rabaey, P.K. Wright, V. Sundararajan, *Pervasive Computing IEEE*, (2005) 28.

20. S. Roundy, P.K. Wright, J. Rabaey, *Energy Scavenging for wireless sensor networks with special focus on vibrations*. ISBN 1-4020-7663-0, Kluwer Academic Publisher, Dordrecht (2004)
21. S. Gea, C.T. Reynolds, N. Roohpour, B. Wirhosentono, N. Soykeabkaew, E. Bilotti, T. Peijs, *Bioresource Technology* 102 (2011) 9105-9110.
22. L. Segal, J.J. Creely, A.E. Martin Jr., C.M. Conrad, *Text. Res. J.* 29 (1959) 786-794.
23. M. Moosavi-Nasab, A.R. Yousefi, *World Academy of Science, Engineering and Technology* 44 (2010) 1258-1263.
24. K-C Cheng, J.M. Catchmark, A. Demirci, *Journal of Biological Engineering* 3 (2009).
25. W. Czaja, A. Krystynowicz, S. Bielecki, R.M. Brown Jr, *Microbial cellulose - the natural power to heal wounds*, *Biomaterials* 27 (2006) 145-151.
26. F. Esa, S.M. Tasirin, N.A. Rahman, *Agriculture and Agricultural Science Procedia* 2 (2014) 113-119.
27. S. Vitta, V. Thiruvengadam, *Current Science*, 102 (2012), 1398-1405.
28. N. Pa'e, N.I.A. Hamid, N. Khairuddin, K.A. Zahan, K.F. Seng, B.M. Siddique, I.I. Muhamad, *Sains Malaysiana*, 43 (2014), 767-773.
29. F. Carrillo, X. Colom, J.J. Suñol, J. Saurina, *European Polymer Journal* 40 (2004) 2229-2234.
30. J. Široký, R.S. Blackburn, T. Betchtold, J. Taylor, P. White, *Cellulose* 17 (2010) 103-115.
31. X. Colom, F. Carrillo, *European Polymer Journal* 38 (2002) 2225-2230.
32. M.L. Nelson, R.T. O'Connor *J. Appl. Polym. Sci.* 8 (1964a) 1311-1323.
33. M.L. Nelson, R.T. O'Connor, *J. Appl. Polym. Sci.* 8 (1964b), 1325-1341.
34. R.T. O'Connor, E.F. DuPré, D. Mitcham, *Textile Research Journal* 28 (1958) 382-392.
35. S.Y. Oh, D.H. Yoo, Y. Shin, H.C. Kim, H.Y. Kim, Y.S. Chung, W.Ho Park, J.Ho Youk, *Carbohydrate research* 340 (2005) 2376-2391.
36. M. Fan, D. Dai, B. Huang, *Electrical and Electronic Engineering, Fourier Transform-Materials Analysis InTech* 2012. pp. 45-68.
37. N. Terinte, R. Ibbett, K.C. Schuster, *Lenzinger Berichte* 89 (2011) 118-131.

38. M. Poletto, V. Pistor, R.M.C. Santana, A.J. Zattera, *Materials Research* 15 (2012) 421-427.
39. P.K. Gupta, V. Uniyal, S. Naithani, *Carbohydrate Polymers* 94 (2013) 843-849.
40. C. Jiao, J. Xiong, *Bioresources* 9 (2014) 6504-6513.
41. M.C. Amin, A.G. Abadi, H. Katas, *Carbohydrate Polymers* 99 (2014) 180-189.
42. P.R. Chawla, I.B. Bajai, S.A. Survase, R.S. Singhal, *Food Technology and Biotechnology* 47 (2009) 107-124.
43. É. Pecoraro, D. Manzani, Y. Messaddeq, S.J.L. Ribeiro, *Polymers and Composites from Renewable Resources*, Elsevier (2007). pp. 369-383.
44. P. Navard, C. Cuissinat, Cellulose swelling and dissolution as a tool to study the fiber structure, in *Proceedings of 2006 7th International Symposium "Alternative Cellulose: Manufacturing, Forming, Properties"*, Rudolstadt, Germany.
45. S. Zhang, W-C. Wang, F-X. Li, J-Y. Yu, *Cellulose Chem. Technol.* 47 (2013) 671-679.
46. H.M. Santos, C. Lodeiro, J-L. Capelo-Martinez, Wiley-VCH Verlag GmbH & Co. 2009. pp. 1-16.
47. A. Isogai, T. Saito, H. Fukuzumi, *Nanoscale*, 3 (2011) 71-85.
48. J. Klíma, A. Frias-Ferrer, J. González-García, J. Ludvík, V. Sáez, J. Iniesta, *Ultrasonics Sonochemistry* 14 (2007) 19-28.

Chapter 5

Summary of the new scientific results

The essential parts (Chapters 2, 3 and 4), as stand-alone documents, provided descriptions of research works targeted to explore cellulose nanocrystal material and surface properties, to investigate thin film manufacturing processes and micro-energy harvesting product possibilities via dielectrophoretic, quantum-mechanical and FEM modeling and were published in number 1 journals in the field, receiving numerous citations.

Ultra-thin aligned CNCs films were successfully obtained in a convective assembly setup that was used under conditions that favored shear-dominated alignment. The degree of orientation of CNCs in these films was high. CNC alignment was found to depend on a balance of forces that included hydrodynamic (shear and drag), Brownian, surface tension (capillary forces), and electrostatic interactions. Best alignment was obtained in cases where the shear force was dominant by coupling it with a low intensity electric field for CNCs and casting evaporation for CNFs. Studies of CNCs, CNFs do not stop at the film formation possibilities. It is a very widely studied material, can be further surface modified by esterification, etherification, oxidation, silylation, polymer grafting etc, or combination of these techniques, which open new functionalization and products for cosmetics, paints, emulsifiers, absorbers and other application.

The objectives of the analytical and experimental works, conclusions, and the new scientific achievements may be summarized as follows.

Brief rehearsal of the objectives and methodologies:

Chapter 2 describes the ultrathin films formation of cellulose nanocrystals (CNCs) obtained by using a convective assembly setup coupled with a low-strength external AC electric field. The orientation and degree of alignment of the rodlike nanoparticles are controlled by the applied field strength and

frequency used during film formation. Calculated dipole moments and Clausius–Mossotti factors allowed the determination of the critical frequencies, the peak dielectrophoresis as well as the principal orientation of the CNCs in the ultrathin films. Quantum-mechanical modeling allowed the determination of the polarization of an elemental cellulose crystal unit. As a result of the combination of shear forces and low electric field highly ultrathin films with controlled, unprecedented CNC alignment were achieved.

Chapter 3 deals with the piezoelectric response of electric field-assisted shear assembly manufactured thin films of aligned cellulose nanocrystals (CNCs) on mica supports. The relationship between polarization gradients and strain mechanics of the obtained films was examined by monitoring their deflection with an atomic force microscope operated in contact mode. The piezoelectric response of the films was ascribed to the collective contribution of the asymmetric crystalline structure of the cellulose crystals. The magnitude of the effective shear piezoelectric constant (d_{25}) of highly ordered CNC films was determined to be 2.1 \AA/V , which is comparable to that of a reference film of a piezoelectric metal oxide. Moreover a FEM model has been created based on the experimental results to evaluate the piezoelectric behavior of samples in CNC composite cantilever arrangement.

Chapter 4 describes bacterial cellulose (BC) film formation for biomedical or smart material applications. In this chapter, results on purified pretreated BC presented, which was subjected to high intensity ultrasound (HIUS) and was investigated for the development of BC films. The morphological, structural and thermal properties of the obtained films were studied by using FE-SEM, AFM, FT-IR, XRD, TGA and DSC characterizations. Results showed that the most favorable purification treatment was the 0.01 M NaOH at $70 \text{ }^\circ\text{C}$ for 2 h under continuous stirring. The most suitable ultrasound operating conditions were found to be, 1 cm distance of ultrasonic probe from the bottom of the beaker, submerged in cold water bath cooling around $12 \pm 2 \text{ }^\circ\text{C}$. The power (25 W/cm^2), time (30 min), BC concentration (0.1% w/w), amplitude (20 μm) and frequency (20 kHz) were maintained constant.

Summary of the new scientific results: thesis of the dissertation:

1. It has been confirmed that convective shear assembly with low electric field can produce highly oriented (degree of orientation is 88%) ultrathin films of CNCs on mica substrate obtained from chemically digested ramie fibers.
2. It has been confirmed that the orientation of CNCs were depend on AC electric field strength and frequency assuming the dipole moment value for prolate ellipsoids and the Clausius Mossotti factor.
3. It has been confirmed that the low AC electric field strength (800 V/cm, 2 kHz) and negative dielectrophoretic forces are suitable for unprecedented anisotropic, homogeneously oriented ultrathin films of CNCs obtained from chemically digested ramie fibers.
4. It has been confirmed that quantum mechanical polarization approach techniques is now possible to predict the value of the piezoelectric tensor in a computationally complex crystalline material such as cellulose.
5. It has been confirmed firstly that CNCs has a large piezoelectric response, $d_{25}=2.10\text{\AA}/\text{V}$.
6. It has been confirmed that the oriented CNCs thin films induce high electromechanical actuation and strain, which can results high mechano-electrical energy transfer.
7. It has been proved that the electromechanical properties of ultrathin films of CNCs and CNFs can be considered in potential micro-energy harvesting applications given their flexoelectric behavior, biodegradability, and renewability. The energy conversion efficiency can be as high as 7.9% (generated electrical energy/mechanical deformation energy ratio).
8. The developed finite element simulation procedure appears to adequately validate the piezoelectric cantilever structure using cellulose nanocrystals as a piezo layer on it.
9. It has been confirmed that high-power ultrasound is capable to liberate individual nanofibrils from dense bacterial cellulose network suitable for thin film application.

The majority of these research were completed in 2015 with the supplemented work and resulted in numerous peer reviewed scientific publications listed here and presentations at scientific symposia. The works discussed above, received significant international attention and was cited approximately 77 times in highly regarded scientific journals.

- 1) Tsalagkas Dimitrios, Lagaňa Rastislav, Poljanšek Ida, Oven Primož, *Csoka Levente*, Fabrication of bacterial cellulose thin films self-assembled from sonochemically prepared nanofibrils and its characterization. *Ultrasonics Sonochemistry* 28: pp. 136-143. (2016), citation: 3.
- 2) *Csoka L*, Dudić D, Petronijević I, Rozsa C, Halasz K, Djoković V, Photo-induced changes and contact relaxation of the surface AC-conductivity of the paper prepared from poly(ethyleneimine)-TiO₂-anthocyanin modified cellulose fibers, *Cellulose* 22:(1) pp. 779-788. (2015)
- 3) Koutsianitis Dimitrios, Mitani Constantina, Giagli Kyriaki, Tsalagkas Dimitrios, Halász Katalin, Kolonics Ottó, Gallis Christos, *Csoka Levente*, Properties of ultrasound extracted bicomponent lignocellulose thin films, *Ultrasonics Sonochemistry* 23: pp. 148-155. (2015), citation: 4.
- 4) Nagy Veronika, Suleimanov Iurii, Molnar Gabor, Salmon Lionel, Bousseksou Azzedine, *Csoka Levente*, Cellulose - spin crossover particle composite papers with reverse printing performance: A proof of concept, *Journal of Material Chemistry C* 3: pp. 7897-7905. (2015)
- 5) I.C. Hoeger, *L. Csoka*, O.J. Rojas, Assembly of CNC in Coatings for Mechanical, Piezoelectric and Biosensing Applications. In: Michael T Postek, Robert J Moon, Alan W Rudie, Michael A Bilodeau (ed.). *Production and Applications of Cellulose Nanomaterials*. Atlanta: TAPPI Press, 2013. pp. 71-74. (ISBN:978-1-59510-224-9)
- 6) *Csoka L*, Appel TR, Eitner A, Jirikowski G, Makovitzky J., Polarization optical-histochemical characterization and supramolecular structure of carbohydrate fibrils, *Acta Histochemica* 115:(1) pp. 22-31. (2013)
- 7) Katalin Halasz, *Levente Csoka*, Plasticized biodegradable poly(lactic acid) based composites containing cellulose in micro and nano size, *Journal of Engineering* 1:(1) pp. 1-9. (2013), citation 15.
- 8) *Csoka L*, Hoeger I, Rojas OJ, Peszlen I, Pawlak JJ, Peralta PN, Piezoelectric Effect of Cellulose Nanocrystals Thin Films, *ACS Macro Letters* 1: pp. 867-870. (2012), citation 29.

- 9) *Csoka L*, Hoeger I, Peralta P, Peszlen I, Rojas OJ, Dielectrophoresis of cellulose nanocrystals and alignment in ultrathin films by electric field-assisted shear assembly, *Journal of Colloid and Interface Science* 363:(1) pp. 206-212. (2011), citation: 26.
- 10) *Csoka L*, Hoeger I, Rojas OJ, Cellulose nanocrystal dielectrophoresis and microfluidic systems, ACS Annual Conference, Los Angeles, CA, USA 241: p. 101-CELL. 1 p. (2011)
- 11) *L Csoka*, P Peralta, I Peszlen, I Hoeger, O Rojas, G Grozdits, Electric field oriented assembly of ultra thin film cellulose nanocrystals, 13th International Conference on Organized Molecular Films, Quebec City, Canada, July 18-21., (2010)
- 12) *L Csoka*, P. Peralta, I. Peszlen, I. Hoeger, O.J. Rojas, Ultra thin films of oriented cellulose nanocrystals by electric field-assisted convective assembly, Espoo, Finland, Tappi Press, 2010. 20 p. (International Conference on Nanotechnology for the Forest Products Industry 2010)(ISBN:9781618390011)

In the peer-reviewed publication above, the author of this dissertation is the corresponding author in the 1st, 3rd, 4th, 6th, 8th and 9th article.

5.1. Final closure

The author sincerely hopes that the works presented here contributed to a certain extent to the better understanding and thoughtful utilization of cellulose nanocrystals and thin films or coating products from it.

Vitae

Levente Csóka was born in Székesfehérvár, Hungary in 1975. He graduated from the Kozma Lajos Technical High School in 1994. After two and half years of musical conservatory studies, he enrolled at the University of Forestry and Wood Sciences, College of Wood Sciences in Sopron, Hungary. He graduated as a MSc, engineer of wood science and technology in 2002. He joined the Institute Wood and Paper Technology in 2003. After one year of researcher work at the Institute of Wood Technology, Akita Prefectural University, Japan, he returned to Sopron and assumed the position of assistant professor at the University of West Hungary (UWH).

To complement his education, he graduated as a MSc, engineer of paper technology in 2005. He received his Ph.D. in Material Science and Technology in 2007. He gained international experiences and participated several education programs in Finland, India, Japan, Canada and USA.

He completed his post-doctoral fellowship at North Carolina State University, Raleigh, USA, in 2010. In 2012, he acquired his “habilitation” at the same institute in Sopron UWH. Currently, he holds the position of associate professor at the Institute of Wood Based Products and Technologies, University of West Hungary, Sopron.

Sopron, April 2016.

Levente Csóka